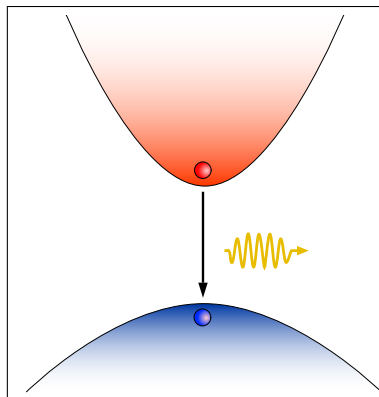# Master Experimental Physics

Electron-induced carrier dynamics in semiconductors

MASTER THESIS

Marnix Christiaan Willem Vreugdenhil BSc.

Supervisors:

M. Solà Garcia MSc. DAILY SUPERVISOR
AMOLF

Prof. Dr. A. Polman SUPERVISOR
AMOLF

Dr. D. van Oosten SUPERVISOR
Utrecht University

27 September 2020

Abstract

In the recent years, there has been a lot of research focused on new photovoltaic materials, complementary to Si-based technologies. In order to improve their efficiency, a fundamental understanding of the excitation and recombination mechanisms of charge carriers in materials is needed. In this work, we investigate carrier dynamics of Cu_2ZnSnS_4 (CZTS) and GaAs using fast electrons as the excitation source, in contrast to previous experiments in which carriers are optically induced. Our results are largely based on time resolved single photon counting measurements. The fast electrons are generated by a femtosecond laser-driven scanning electron microscope which generates pulses consisting of (statistically) less than one electron up to 1200 electrons per pulse at voltages between 5 and 30 kV. We analyze our results both qualitatively and quantitatively by considering Auger, radiative, Shockley-Read-Hall and Surface recombination. For CZTS, we have found a value of $B = (4.8 \pm 0.2) \cdot 10^{-10} cm^3 s^{-1}$ for the bimolecular coefficient in optical experiments. We observe that this value becomes variable as a function of number of electrons per pulse in fast electron experiments: $B \propto N_e^{-1.1}$. In the case of GaAs, the model does not show a good fit with the data. However, we distinguish two main decay mechanisms, one in a short timescale (up to 0.5 ns) and a second one in the longer timescale (tens of ns), which we attribute to Shockley-Read-Hall recombination.

Contents

1 Introduction

Our society currently still relies very much on the use of fossil fuels for energy. One of the ways to decrease our dependence on fossil fuels is to switch to more renewable energy sources, like solar energy. Silicon-based solar cells are currently still the most abundant type of solar cell, but there are downsides to using Si-based solar cells, like their weight per m^2. Much research is therefore constantly being done into finding alternatives to Si-based solar cells.

One relatively new type of solar cell is that based on quaternary semiconductor compounds. $CuIn_xGa_{(1-x)}Se_2$ (CIGS) solar cells currently hold the efficiency record, $\eta = 21.7\%$, in this category. [1] This material has the problem however, that it contains some rare elements, making it very costly and problematic for large scale use.

Recently, another material in this category has gained a lot of attention, namely Cu_2ZnSnS_4 (CZTS). This material is very promising due to a number of reasons. Firstly, it is a direct band gap semiconductor with a band gap energy of approximately 1.5 eV, making it ideal for use in solar cells. [2] Moreover, it has a large absorption constant, on the order of $10^4 \, cm^{-1}$. [3] This means that the material can be used for thin-film solar cells. Lastly, it consists of only earth-abundant elements, giving it the possibility of being manufactured on a large scale at a relatively low price. The current efficiency record of a CZTS solar cell stands at 12.6%. [1]

To increase the efficiency of CZTS solar cells, it is important to know more about the carrier dynamics in the material. This has already been studied to some extend with optical excitation, see for instance [4]. One, often overlooked, way to study the carrier dynamics in a material is by excitation using fast electrons. The use of fast electrons might give insights into carrier dynamics, that could not be obtained using optical excitation. One reason for this is that much smaller volumes of the material can be excited using fast electrons.

A new technique to study ultrafast processes after electron excitation is by means of a femtosecond laser-driven scanning electron microscope (SEM). [5][6][7] Our research group has such an SEM and the setup that this is a part of is specialized for measuring cathodoluminescence (CL). As an added advantage, our setup can excite a material with both fast electrons and femtosecond laser pulses at the same spot, either simultaneously, or with a delay between excitations. This means that the setup can also be used to measure photoluminescence (PL). The setup can be used for both measuring luminescent spectra, and for time resolved measurements.

This research will focus on describing the fast electron induced carrier dynamics in CZTS. We will also study the carrier dynamics due to optical excitation in CZTS. These measurements will be useful since much more is known about PL than about CL. A significant portion of this work will also be focused on studying the carrier dynamics, due to both optical excitation and excitation by fast electrons in GaAs. Very much is already known about the carrier dynamics in GaAs, and it will therefore provide a good reference for our CZTS measurements. GaAs has the added advantage that it is a direct band gap semiconductor with a band gap energy which is similar to that of CZTS (namely 1.43 eV). [8] We hypothesize that the carrier dynamics can be well-described using a model that is based on a combination of Auger, radiative, Shockley-Read-Hall (SRH) and surface recombination.

The current thesis is divided into several parts. We will first provide a theoretical framework which we will later use to analyze our data. In this framework, we will discuss the generation of charge carriers in semiconductors due to both optical excitation and to excitation by fast electrons, together with the main recombination mechanisms (SRH, bimolecular, Auger and surface recombination). We will continue by describing what the temporal evolution of a luminescent signal looks like in several cases and, lastly, present a number of numerical simulations of carrier dynamics.

After we have provided a theoretical framework, we will discuss the experimental setup. This explanation first describes the SEM, its sample chamber and the optical setup. We then explain how the SEM can be driven by a femtosecond laser to produce short pulses of electrons. Finally, we will discuss the concept of time resolved single photon counting measurements, as this type of measurement is central to the thesis.

We continue the thesis by describing our experimental results. First, we will present the data that we have gathered from our CZTS sample. The analysis includes several surprising effects, like a variable bimolecular coefficient, that have never been presented before. We conclude the results section by presenting the data gathered from our GaAs sample.

In the last section of this work, we will summarize our experiments and results. This section will also include an outlook for future research.

2 Theory

In this work, we aim to describe the temporal evolution of the charge carrier density in semi-conductors after excitation with pulses of electrons. We will look specifically at intrinsic bulk semiconductors with a direct band gap.[1] All our measurements are based on measuring the luminescence that is produced by the sample as a result of the excitation. In this chapter, we explain the theory behind free charge carrier generation and recombination.

The charge carriers that are relevant for semiconductors (and therefore relevant for this work) are conduction band (free) electrons and holes. We will denote the density of free electrons at time t (s) at position $\mathbf{r} = (x, y, z)$ (cm) with $n(\mathbf{r}, t)$ and the density of holes with $p(\mathbf{r}, t)$ (both in cm^{-3}). In general we would expect these quantities to be described by the following differential equations:

$$\frac{\partial n(\mathbf{r}, t)}{\partial t} = G_n(\mathbf{r}, t, ...) - R_n(n(\mathbf{r}, t), p(\mathbf{r}, t), \mathbf{r}, t) - D_n \nabla^2 n(\mathbf{r}, t), \tag{1}$$

$$\frac{\partial p(\mathbf{r}, t)}{\partial t} = G_p(\mathbf{r}, t, ...) - R_p(n(\mathbf{r}, t), p(\mathbf{r}, t), \mathbf{r}, t) - D_p \nabla^2 p(\mathbf{r}, t). \tag{2}$$

Here $G_n(\mathbf{r}, t, ...) \equiv G_n$ and $G_p(\mathbf{r}, t, ...) \equiv G_p$ are the generation rates for conduction electrons and holes respectively $(cm^{-3}s^{-1})$.
Equivalently $R_n(n(\mathbf{r}, t), p(\mathbf{r}, t), \mathbf{r}, t) \equiv R_n$ and $R_p(n(\mathbf{r}, t), p(\mathbf{r}, t), \mathbf{r}, t) \equiv R_p$ are the recombination rates of electrons and holes respectively $(cm^{-3}s^{-1})$. Finally, D_n and D_p are the diffusion coefficients of free electrons and holes respectively. (cm^2s^{-1}).
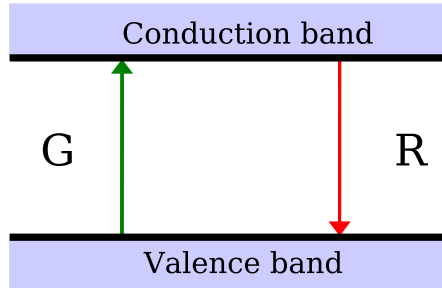
Figure 1: Schematic of generation and recombination.

As a first approximation, we might assume diffusion to only play a small role. In this case, we can also assume that $n(\mathbf{r}, t) = p(\mathbf{r}, t)$ since we consider an intrinsic semiconductor. Using this approximation, equations 1 and 2 reduce to

$$\frac{\partial n}{\partial t} = G - R, \tag{3}$$

---

[1]We do our experiments on GaAs and Cu_2ZnSnS_4 (CZTS), but this theory applies to other intrinsic direct band gap semiconductors as well.

for $n \equiv n(\mathbf{r}, t)$. Most of the remainder of this chapter will be focused on determining G and R.

2.1 Generation of carriers

Our first objective is to determine the generation rate G $(cm^{-3}s^{-1})$ from equation 3. This is the rate at which electron-hole (e-h) pairs are created. Many mechanisms can contribute to the generation of e-h pairs in semiconductors, but we will only discuss the three mechanisms that are most relevant for this work. These mechanisms are visualized in figures 2 (a), (b) and (c).
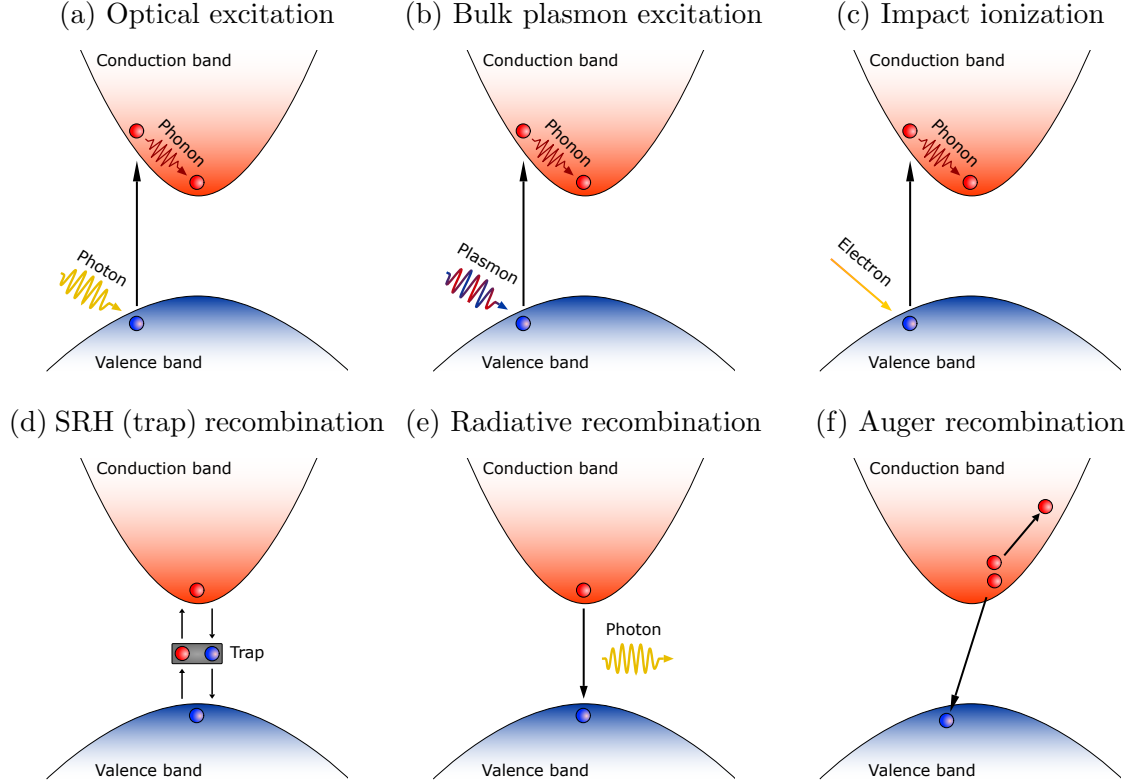
Figure 2: Types of e-h pair generation and recombination. The blue circles represent holes and the red circles represent conduction band (free) electrons.

2.1.1 Optical excitation

Consider a photoluminescence experiment where we irradiate our sample using a pulsed laser at a wavelength λ with a repetition rate R_{rep}. We will also assume a relatively low laser fluence such that the light intensity in the sample is well described by the Beer-Lambert law. Given some initial light intensity $I_0(x, y, z = 0) = I_0$ for a collimated beam propagating through our sample in the positive z-direction, the intensity $I(x, y, z) = I(z)$ will be given by

$$I(z) = I_0 T(z) = I_0(A - 1) = I_0 e^{-\alpha(\lambda)z}. \tag{4}$$

Here, $T(z) \equiv T = I(z)/I_0$ is the transmittance, $A = 1 - T$ is the absorbance and $\alpha(\lambda)$ is the absorption coefficient (cm^{-1}).

The Beer-Lambert attenuation can be classically interpreted to come from the wavenumber of the electric and magnetic fields in the material. If the frequency of the light is close to some resonant frequency of the (valence electrons of) material, the complex component of the wavenumber k will become large and the electric and magnetic fields will be attenuated [9, pp. 417-424]. The absorption coefficient is then given by $\alpha = 2 \operatorname{Im}(k)$ (since the intensity is proportional to the square of the electric field).

λ (nm)	E_{ph} (eV)	α_{GaAs} (cm^{-1}) [10]	α_{CZTS} (cm^{-1}) [3]	n_{GaAs}; $R_\perp$ [11]	n_{CZTS}; $R_\perp$ [12]
345	3.59	$7.17 \cdot 10^5$	$1.24 \cdot 10^4$	3.497; 0.31	2.67; 0.21
517	2.40	$9.02 \cdot 10^4$	$1.24 \cdot 10^4$	4.203; 0.38	2.14; 0.13

Table 1: Literature values of the absorption coefficients for GaAs and CZTS at the wavelengths that we use in our experiments. Note especially that GaAs is much more opaque for $\lambda = 345$ nm than it is for $\lambda = 517$ nm. The refractive indices ($n_{GaAs,CZTS}$) and the corresponding reflectances at normal incidence ($R_\perp$) (according to equation 5) are also given.

So far, we have only considered a beam traveling through a single material, but for the purposes of our experiments, it is also useful to consider a beam that passes some interface between materials. Considering this case allows us to also describe the partial reflection that occurs at this interface. The reflectance R (at normal incidence) at an interface separating two materials, with refractive indices n_1 and n_2 respectively, is given by Fresnel's equation

$$R = \left| \frac{n_1 - n_2}{n_1 + n_2} \right|^2. \tag{5}$$

Let us now reconsider the situation on which equation 4 is based, but assume the beam to travel from vacuum to the material, with the interface at $z = 0$. The intensity of the beam traveling through vacuum is now given by I_0, but since there is reflection at the interface, equation 4 is now rewritten as

$$I(z > 0) = (1 - R)I_0 e^{-\alpha(\lambda)z} = \frac{4n}{(n+1)^2} I_0 e^{-\alpha(\lambda)z}, \tag{6}$$

where n is simply the refractive index of the material.

If we irradiate some material using a pulsed laser, the energy density (energy per unit volume) at penetration depth z is given by

$$\Phi(z) = \frac{\alpha(1-R)Pe^{-\alpha z}}{R_{rep}S}, \tag{7}$$

where P is the average laser power and S is the cross section of the laser beam. Table 1 shows the absorption coefficients for the materials that we focus on in this work at the wavelengths that we use during our PL experiments. For later reference, equation 7 has been plotted for

5

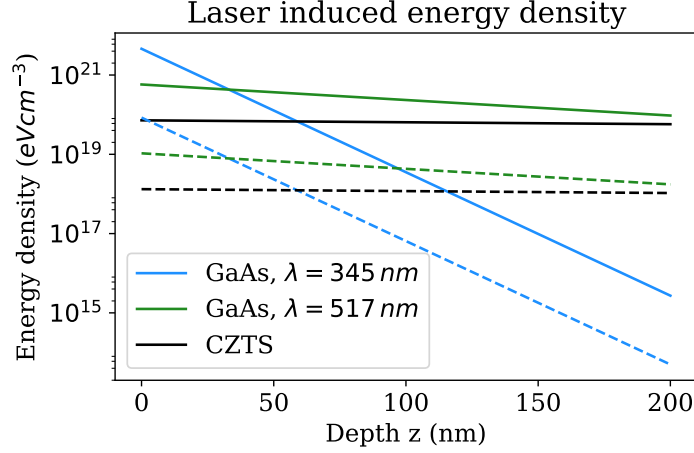these materials at two typical laser fluences in figure 3.

Figure 3: Laser induced energy densities according to the Beer-Lambert law. The solid lines correspond to a laser fluence of $1.03 \ mJcm^{-2}$ and the dashed lines to $0.019 \ mJcm^{-2}$. These fluences correspond to typical laser fluences used in our experiments. See table 1 for the absorption coefficients that were used to plot the figure.

Approximation: square pulse

So far we have only looked at energy absorption in a semiconductor, but our goal is to determine the generation rate. To do this we will replace the classical interpretation of absorption summarized above with a quasi-quantum interpretation of absorption. In this picture, a valence band electron can absorb a photon to be promoted to the conduction band.[2] This process is visualized in figure 2 (a). For this process to occur, the photon energy $E_{ph} = \hbar\omega$ must exceed the band gap energy E_g. If this requirement is met, the generation rate due to this single photon absorption will be proportional to the number of photons N_{ph} in a pulse.

We can approximate the z-dependent generation rate by considering a pulsed laser that generates square monochromatic parallel (non-converging) pulses as our source. The laser generates pulses at a wavelength λ, with pulse duration Δt at a repetition rate R_{rep}, with a cross section S and an average power P such that $I_0 = P/S$. A single pulse will then have an energy $E_{pulse} = P/R_{rep} = I_0/(SR_{rep})$. Given a photon energy $E_{ph} = hc/\lambda$ (where h is the Planck constant and c is the speed of light), the number of photons in a single pulse will be given by

$$N_{ph} = \frac{E_{pulse}}{E_{ph}} = \frac{P\lambda}{hcR_{rep}}. \tag{8}$$

Not all photons that are absorbed by the material will necessarily be absorbed by valence band electrons, so we denote the absorption efficiency (or probability) of a valence band

---

[2]In this picture, the absorption coefficient can be interpreted as being the product of the absorption cross section and the density of valence electrons: $\alpha = \sigma\rho_v$.

electron with Q. We also need to include a factor $(1 - R) = 4n_r/(n_r + 1)^2$ (where $n_r \equiv n_r(\lambda)$ is the refractive index of the semiconductor) to account for the reflection at the interface between vacuum and the semiconductor. For simplicity, we will however define the *absorbed* power as $P_{abs} \equiv (1 - R)P$. The number of electron-hole pairs N_e that are created in a volume $V = S \cdot (z_2 - z_1)$ is[3]

$$N_e = (1 - R)QN_{ph}\alpha \int_{z_1}^{z_2} T(z)\,dz = \frac{P_{abs}\lambda Q\alpha}{hcR_{rep}} \int_{z_1}^{z_2} e^{-\alpha z}\,dz. \tag{9}$$

The corresponding average electron density in this volume is simply $n = N_e/V = N_e/S \int_{z_1}^{z_2} dz$. Given our pulse duration Δt, the generation rate becomes

$$G = \frac{(1 - R)N_e}{V\Delta t} = \frac{QP_{abs}\lambda\alpha}{hc\Delta tR_{rep}} \frac{\int_{z_1}^{z_2} e^{-\alpha z}\,dz}{S \int_{z_1}^{z_2} dz}. \tag{10}$$

Filling in $z_1 = z$ and $z_2 = z + dz$, we get the z-dependent generation rate:

$$G(z) = \frac{(1 - R)QP\lambda\alpha}{hc\Delta tR_{rep}S}e^{-\alpha z}. \tag{11}$$

Note that this equation is expressed only in terms of measurable quantities (apart from Q) and constants of nature. If we fill in $Q = 1$, equation 11 gives us an upper limit to the generation rate.

2.1.2 Electron-induced generation and bulk plasmons

Electron-hole pairs can also be generated by injecting highly energetic electrons into the system. As it travels through the material, the incoming electron loses its energy through inelastic scattering events. Most of its energy is lost through the production of so-called bulk plasmons. [13][14, pp. 5-8][15] Bulk plasmons are the quantization of oscillations in the valence electron plasma[4] of a semiconductor. [8, pp. 401-402] These oscillations are caused by the movement of the incoming highly energetic electron through the material. This incoming electron displaces the valence electron gas due to the repulsive Coulomb force. Displacement of the valence electrons results in the incoming electron being trailed by a so-called correlation hole: a region of net-positive charge. [14, pp. 5-8] The quantized energy of the subsequent plasma oscillation is given by [16][14]

$$E_p = \hbar\sqrt{\frac{e^2 n_e}{\epsilon_0 m^*}}. \tag{12}$$

Here e is the electron charge, n_e is the atomic electron density, m^* is their effective mass and ϵ_0 is the vacuum permittivity.

---

[3]To see the validity of this equation, it might help to evaluate the integral: $N_e = (1 - R)QN_{ph}(e^{-\alpha z_1} - e^{-\alpha z_1})$. It is clear that this is the number of electron-hole pairs generated between z_1 and z_2.

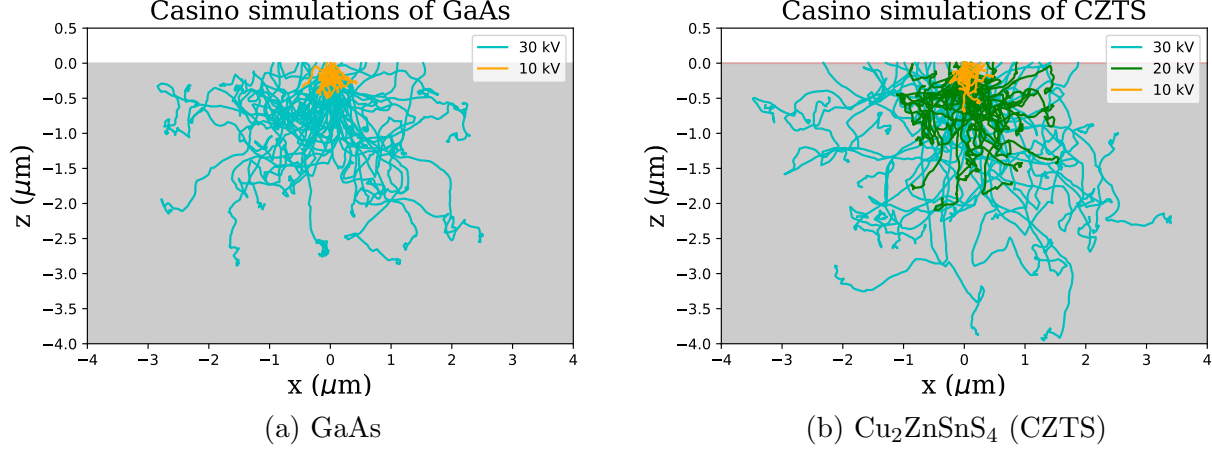[4]In the case of metals, plasmons are oscillations in the free electron plasma.

Figure 4: CASINO simulations of electron cascades in GaAs (a) and CZTS (b). The trajectories are projected onto the xz-axis. Each vertex in a trajectory represents a scattering event. The blue cascades correspond to 30 keV, the green to 20 keV and the orange to 10 keV electrons. For the GaAs simulations, the average plasmon energy used to simulate the trajectories was 15.9 eV [14]. To the best of our knowledge, the plasmon energy of CZTS has never been measured. We have therefore used the theoretical value of 13 eV (according to equation 12). Our CZTS sample is covered by a 3 nm layer of Al_2O_3 (which has a plasmon energy of 21 eV [14, p. 7]), so this was also added to the simulation. As can clearly be seen from these simulations, the scattering events of 10 keV electrons are localized to a very small volume. This volume increases rapidly with increasing electron energy.

At each scattering event, the incoming electron loses some of its energy and changes it direction. Electron trajectories can be simulated using "CASINO" (version 3.3.0.4) Monte Carlo simulations. [17] Figure 4 shows the projections on the xz-axis of such trajectory simulations for the materials that we work with in this work.

(a) GaAs, 10 keV

(b) GaAs, 30 keV

(c) CZTS, 5 keV
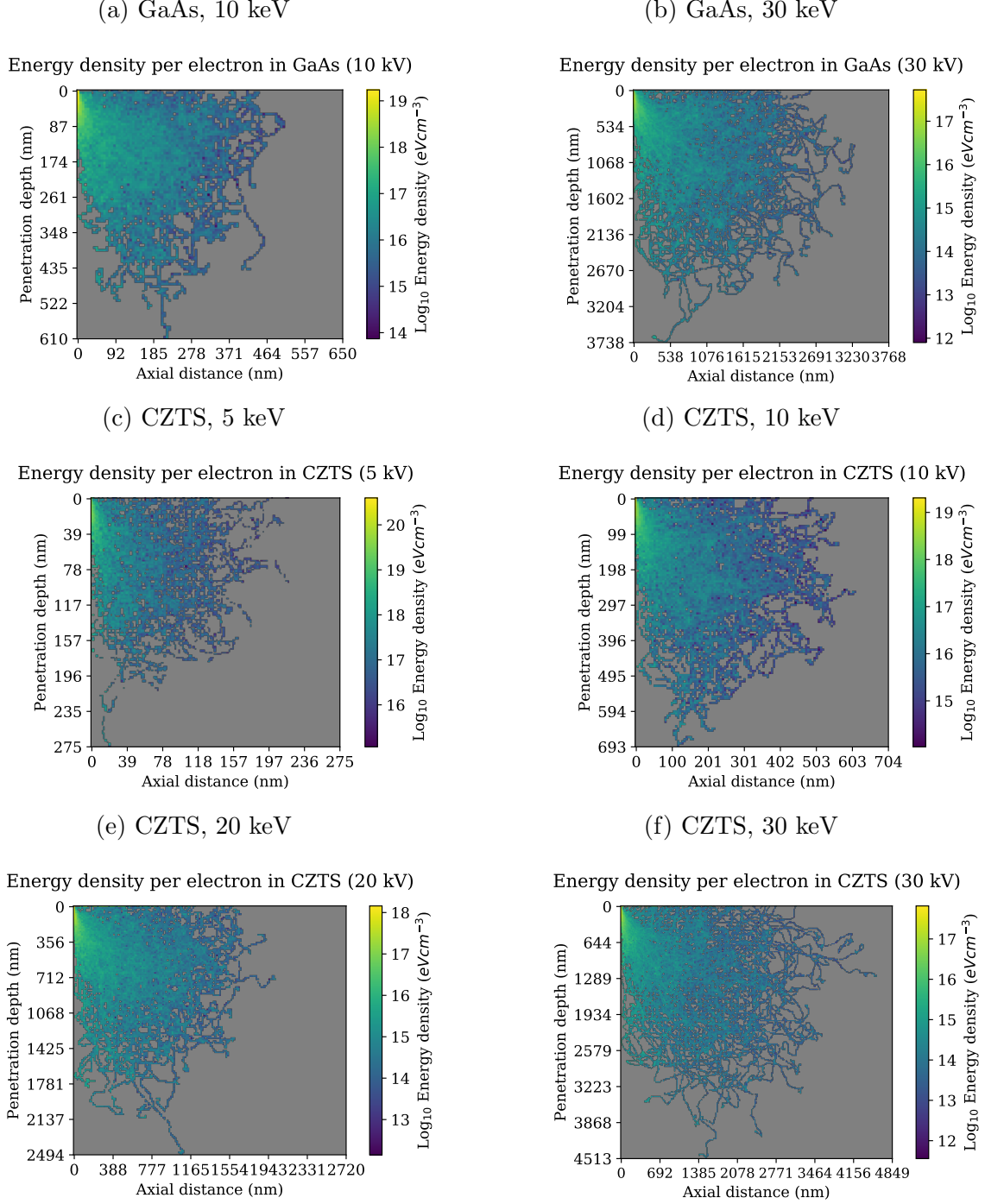
(d) CZTS, 10 keV

(e) CZTS, 20 keV

(f) CZTS, 30 keV

Figure 5: Average energy density profile *per electron*, for GaAs and CZTS after excitation by highly energetic electrons. These were determined using CASINO simulations. The areas of high energy density are roughly pear-shaped. Note that the values on the axes and the color bars differ for each plot.

These simulations can also be used to study the energy distribution as deposited by fast electrons. By simulating incoming electrons at 10 kV and 30 kV for GaAs and at 5 kV, 10

kV, 20 kV and 30 kV for CZTS[5] (1000 electrons per simulation), we have determined the induced energy densities as a function of penetration depth and axial distance. We have done so by dividing up the cascade volume into ring-shaped volumes, each with a unique z (depth) and r (radial distance) component. For each of these volumes, we sum up all energy lost in scattering events in that volume. Then, we divide these sums by the size of the associated volume and by the number of electrons used in the simulation (1000). This leaves us with a distribution of the average deposited energy density per electron, as a function of z and r. These energy densities are shown in figure 5. The CASINO simulations clearly show that the peak energy density decreases for increasing acceleration voltage. Table 2 shows the simulated maximum energy densities per electron.

Material	Initial energy (keV)	Peak energy density ($eV cm^{-3}$)	Φ_{peak}/E_g (cm^{-3})
CZTS	5	$4.0 \cdot 10^{20}$	$2.6 \cdot 10^{20}$
CZTS	10	$2.0 \cdot 10^{19}$	$1.4 \cdot 10^{19}$
CZTS	20	$1.4 \cdot 10^{18}$	$9.6 \cdot 10^{17}$
CZTS	30	$6.6 \cdot 10^{17}$	$4.4 \cdot 10^{17}$
GaAs	10	$1.7 \cdot 10^{19}$	$1.2 \cdot 10^{19}$
GaAs	30	$5.3 \cdot 10^{17}$	$3.7 \cdot 10^{17}$

Table 2: Peak energy densities according to our CASINO simulations. The last column shows the peak energy density divided by the band gap energy (1.5 eV and 1.43 eV for CZTS [2] and GaAs [8, p. 190] respectively). This is the energetic upper limit of the peak induced carrier density.

Dividing the energy densities by the band gap energy of the material yields an upper limit to the induced carrier density per incoming electron. The energy densities in figure 5 can also be divided by the average plasmon energy[6] to estimate the average bulk plasmon density per electron.

A bulk plasmon usually decays into a single e-h pair (see figure 2 (b)). [13][18] Depending on the plasmon energy $\hbar\omega_p$ and the band gap energy E_g of the material, the electron and hole might have enough energy to excite one or several additional e-h pairs. This happens through a process called impact ionization[7], which is visualized in figure 2 (c). So even though a plasmon only decays into a single e-h pair, several more subsequent pairs might be created as an indirect result of this decay. It is difficult to accurately determine the number of e-h pairs that are created per plasmon and there is not a lot of literature on this. Following reference [19, Table 1], we will assume that 1 plasmon in GaAs will on average excite 3 e-h pairs. Using the theory provided in the same paper, we expect the number of created e-h pairs per plasmon in CZTS to also be around 3. [19, Eq. 3]

---

[5]These acceleration voltages correspond to the CL experiments we have done.

[6]13 eV and 15.9 eV for CZTS and GaAs respectively.

[7]When impact ionization occurs several times due to one electron, it is also sometimes referred to as avalanche ionization. [20]

2.2 Recombination

Once an excess of e-h pairs is created in the semiconductor, the system is in a state of non-equilibrium. The equilibrium is restored through the combination of several recombination processes. Our objective in this section is to determine the recombination rate R ($cm^{-3}s^{-1}$) from equation 3. The total recombination rate can be described in terms of the combined effects of Shockley-Read-Hall (trap), radiative and Auger recombination:

$$R = R_{SRH} + R_r + R_A, \tag{13}$$

where R_t, R_r and R_A are the trap, radiative and Auger recombination rates respectively.
It is important to realize that these rates are not constants, but that they can depend on several parameters. The following subsections will each focus on a single recombination mechanism. They will however share some common nomenclature which we will briefly discuss here. Conduction band electron density is denoted with $n(t) = n_0 + \Delta n(t)$ and similarly, the hole density with $p(t) = p_0 + \Delta p(t)$.[8] Here n_0 and p_0 are the equilibrium free electron and hole densities[9] respectively and $\Delta n(t)$ and $\Delta p(t)$ are the excess densities. Furthermore, just after excitation, the carrier densities are given by $n(t = 0) = n_0 + \Delta n_0$ and $p(t = 0) = p_0 + \Delta p_0$.

2.2.1 Shockley-Read-Hall recombination

We will first consider Shockley-Read-Hall (SRH) recombination. This type of recombination relies on the presence of so-called traps in the material. These are energy levels located within the band gap of the material and may, for instance, be due to impurities. SRH recombination is visualized in figure 2 (d). If we consider a semiconductor at temperature T, with Fermi level $E_F \approx E_g/2$ and with a trap density N_t at an energy E_t, the SRH recombination rate is given by [21]

$$R_{SRH} = \frac{\sigma_n \sigma_p v_{th} (np - n_0^2) N_t}{\sigma_n(n + n_i e^{\Delta E/k_B T}) + \sigma_p(p + n_i e^{-\Delta E/k_B T})}. \tag{14}$$

Here, $\Delta E \equiv E_t - E_F$ is the energy difference between the trap and the Fermi level, σ_n and σ_p are the electron and hole cross sections respectively and $v_{th} \equiv \sqrt{3k_B T/m^*}$ is the thermal velocity (which we assume to be the same for electrons and holes) with effective mass m^*. Since equation 14 is quite complicated, it might be useful to look at the situation of an intrinsic semiconductor, where $p = n = n_0 + \Delta n$ and $\sigma_n = \sigma_p \equiv \sigma$. In this case the expression reduces to

$$R_{SRH} = \frac{1}{2} \frac{(\Delta n^2 + 2\Delta n n_0) N_t \sigma v_{th}}{\Delta n + n_0 \left[1 + \cosh\left(\frac{E_t - E_F}{k_B T}\right)\right]}. \tag{15}$$

If we now define the SRH lifetime as $R_{SRH} = \Delta n/\tau_{SRH}$, it will be given by

$$\tau_{SRH} = 2 \frac{\Delta n + n_0 \left[1 + \cosh\left(\frac{E_t - E_F}{k_B T}\right)\right]}{(\Delta n + 2n_0) N_t \sigma v_{th}}. \tag{16}$$

---

[8]Sometimes we use the shorthand notation $n \equiv n(t)$, $p \equiv p(t)$, $\Delta n \equiv \Delta n(t)$ and $\Delta p \equiv \Delta p(t)$.
[9]You might also often encounter the following definition in literature: $n_0 p_0 = n_i^2$.

For *small deviations* from equilibrium $n_0 \gg \Delta n$, the lifetime is independent of the carrier density and the trap recombination rate reduces to

$$R_{SRH} \approx \Delta n \frac{N_t \sigma v_{th}}{1 + \cosh\left(\frac{E_t - E_F}{k_B T}\right)}. \tag{17}$$

Part of this expression is often defined as the minority carrier lifetime: $\tau_{min} = (N_t \sigma v_{th})^{-1}$. In the case where the trap level is close to the middle of the band gap ($E_t \approx E_F$), the trap recombination rate (for $n_0 \gg \Delta n$) will become $R_{SRH} \approx \Delta n / 2\tau_{min}$.
If the deviation from equilibrium is very large ($\Delta n \gg n_0$), the rate will become

$$R_{SRH} \approx \frac{\Delta n^2 N_t \sigma v_{th}}{\Delta n + n_0 \left[1 + \cosh\left(\frac{E_t - E_F}{k_B T}\right)\right]}. \tag{18}$$

Here again, we can look at the case where the trap is approximately at mid-band level, such that the second term in the denominator becomes very small compared to the first term. This means that the large excitation recombination rate will approximate $R_{SRH} \approx \Delta n / \tau_{min}$.

2.2.2 Bimolecular recombination

We will now look at the second term in equation 13: R_r, the radiative (or bimolecular) recombination rate. This process can be interpreted as the inverse of single photon absorption. During a radiative recombination event, an electron near the bottom of the conduction band recombines with a hole at the top of the valence band, while emitting a photon (see figure 2 (e)). Since radiative recombination requires a free electron and a hole to be present, the rate at which it occurs is proportional to the product of their densities: [22][23, pp. 87-89]

$$R_r = Bnp, \tag{19}$$

where B is the bimolecular recombination coefficient ($cm^3 s^{-1}$). For the case of a high excitation level ($\Delta n \gg n_0$ and $\Delta p \gg p_0$) and an intrinsic semiconductor ($n = p$), the radiative recombination rate can be written as $U_r = B\Delta n^2$. If $G = 0$ and radiative recombination is the dominant recombination process ($R_r \gg R_A$, R_t), then equations 3 and 19 reduce to

$$\frac{\partial n}{\partial t} = \frac{\partial \Delta n}{\partial t} \approx B\Delta n^2, \tag{20}$$

which has the following solution:

$$n(t) = n_0 + \frac{\Delta n_0}{B\Delta n_0 t + 1}. \tag{21}$$

Since radiative recombination is usually only dominant when[10] $\Delta n \gg n_0$, the n_0 term is often left out of this expression.

---

[10]For direct band gap semiconductors, a typical value for B is around $10^{-10} cm^3 s^{-1}$ and a typical τ_{SRH} might be on the order of tens of ns. In this case, for $\Delta n \approx 10^{16}$, $R_{SRH} \gg R_r$, for $\Delta n_0 \approx 10^{18}$, $R_{SRH} \approx R_r$ and for $\Delta n_0 \approx 10^{20}$ $R_{SRH} \ll R_r$.

The bimolecular coefficient is usually treated like a constant [24], however there are mechanisms through which it can vary. One well known dependency of the B coefficient is temperature [25, pp. 18-20][26], although it seems unlikely that the temperature dependence plays a significant role in our experiments. Some works have reported a *carrier density* dependence of B however. [27][28][29] It must be noted though, that the materials researched in these papers are specific types of quantum wells. They are therefore significantly different from the samples the we investigate in this work.

2.2.3   Auger recombination

Auger recombination is the process where an electron and a hole recombine and give off their excess energy to a third carrier. It can be interpreted as the inverse of impact ionization and is visualized in figure 2 (f). The process can either involve two electrons and one hole or two holes and one electron. The Auger recombination rate is therefore given by [24]

$$R_A = C_n n^2 p + C_p n p^2. \tag{22}$$

Here C_n and C_p are the Auger coefficients for the two Auger processes described above respectively. When looking at the case of high excitation and an intrinsic semiconductor again, this rate reduces to $R_A = Cn^3$ (where C is the *effective* Auger coefficient). If during some time domain, the Auger process is the main recombination mechanism (and there is no generation of carriers), the carrier density will thus be given by

$$n(t) = n_0 + \frac{\Delta n_0}{\sqrt{C \Delta n_0^2 t + 1}}. \tag{23}$$

Auger recombination is usually only dominant for a very short time after excitation due to the n^3 dependence. This is illustrated in figure 6.
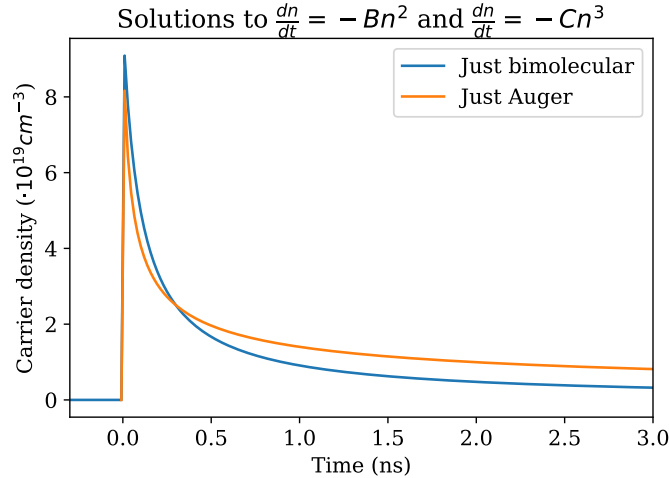

Figure 6: A comparison of decay curves for just bimolecular recombination (equation 21 with $B = 10^{-10} cm^3 s^{-1}$) and for just Auger recombination (equation 23 with $C = 5 \cdot 10^{-30} cm^6 s^{-1}$). During the first 100 ps, the Auger recombination rate is significantly higher than the bimolecular rate. After several hundreds of picoseconds however, the bimolecular recombination rate dominates over the Auger rate.

2.2.4 Surface recombination

One type of recombination we haven't covered yet is surface recombination. As the name implies, this process only occurs near the surface of the material and it is due to the presence of so-called dangling bonds, which serve as energy levels within the band gap of the material. [23, pp. 151-153] Surface recombination in a semi-infinite bulk material (in the region $z \geq 0$) is best described using the diffusion equation [23, pp. 151-153][22]

$$\frac{\partial n}{\partial t} = D\nabla^2 n, \tag{24}$$

with boundary conditions

$$D\frac{\partial n}{\partial z}\Big|_{z=0} = Sn, \tag{25}$$

$$n(z < 0) = n(z \to \infty) = 0. \tag{26}$$

Here D is the ambipolar diffusion coefficient ($cm^2 s^{-1}$) [30], S is the surface recombination velocity ($cm s^{-1}$) and ∇^2 denotes the second order spatial derivative. This set of equations does not provide a simple solution for the recombination rate, but several approximations have been proposed. Some authors approximate the surface recombination rate by treating it like SRH recombination. [31] However, other approximations have also been proposed where the surface recombination lifetime is given by [25, pp. 23-25][32]

$$\tau_s = \frac{D}{S^2}. \tag{27}$$

The quantitative analysis presented in this work will not include surface recombination.

2.3 Luminescent signal

One way to probe the time evolution of the carrier density is to look at the temporal luminescent signal it gives off after excitation. The difficulty with this comes from the fact that we're only probing the *radiative* recombination rate when we do this, so our signal $S(t) = R_r(t) = Bn^2$. [23]

We can get an analytical expression for this $S(t)$ in a small number of special cases. The simplest of these is the case where there is only bimolecular recombination in an intrinsic semiconductor with $\Delta n \gg n_0$. For this special case, the expression for the signal is simply found by squaring equation 21 and multiplying it with B:

$$S(t) = \frac{B\Delta n_0^2}{(B\Delta n_0 t + 1)^2} = \frac{S_0}{(\sqrt{BS_0}t + 1)^2}, \tag{28}$$

where $S_0 \equiv S(t = 0) \approx B\Delta n_0^2$.

We get a different analytical expression for $S(t)$ if we look at the case as described above, but there is *also* some kind of linear recombination (for instance: SRH recombination) with a lifetime τ. The differential equation that needs to be solved in order to get the expression for $S(t)$ is

$$\frac{dn}{dt} = -Bn^2 - \frac{n}{\tau}. \tag{29}$$

14

This is a separable differential equation which has the following solution

$$n(t) = n_0 + \frac{\Delta n_0 e^{-t/\tau}}{1 + B\tau\Delta n_0(1 - e^{-t\tau})}. \tag{30}$$

From this, we can now derive the signal:

$$S(t) = B\Delta n^2 = \frac{B\Delta n_0^2 e^{-2t/\tau}}{(1 + B\tau\Delta n_0[1 - e^{-t/\tau}])^2} = \frac{S_0 e^{-2t/\tau}}{(1 + \tau\sqrt{S_0 B}[1 - e^{-t/\tau}])^2}. \tag{31}$$

Another analytic expression we can get for the luminescent signal is for the case where the carrier concentration is so high that the Auger recombination rate dominates over the other recombination mechanisms. In this case, there still is radiative recombination (so there is still luminescence), but it does not significantly contribute to the total recombination rate. Similarly to the case where there is only radiative recombination (which was discussed at the beginning of this section), we get the expression for the luminescent signal by squaring equation 23 and multiplying it with B:

$$S(t) = B\Delta n_0^2 = \frac{B\Delta n_0^2}{C\Delta n_0^2 t + 1} = \frac{S_0}{\frac{C}{B}S_0 t + 1}. \tag{32}$$

It should be noted that this last equation only holds for the short time domain where[11] $R_A \gg R_r$, R_{SRH} and therefore not for any t.

2.4 Numerical simulations

Equations 1 and 2 can only be solved analytically for a small number of special cases. We can however solve versions of these equations numerically to give insights into the effects that certain recombination mechanisms have. In this section, we will present the numerical simulations of a simplified generation and recombination model, known as the ABC-model. [27, pp. 1-2] We will use the literature values of relevant constants for intrinsic bulk GaAs and realistic experimental parameters in these simulations.

2.4.1 ABC-model simulations

The model that we use for our numerical simulations includes three types of recombination, namely SRH, bimolecular and Auger recombination. It does not include diffusion or surface recombination. The differential equation (DE) that we solve for these simulations is therefore given by

$$\frac{dn}{dt} = G - An - Bn^2 - Cn^3. \tag{33}$$

Here, G is the generation term, A is the inverse of the SRH lifetime ($A = 1/\tau_{SRH}$) and B and C are the bimolecular and Auger coefficients respectively. The DE is made iterative to be able to use it for numerical simulations

$$n_i = n_{i-1}(1 - \Delta t(Cn_{i-1}^2 + Bn_{i-1} + [1/\tau])) + \Delta t G_i, \tag{34}$$

---

[11]The Auger coefficient typically has a value of approximately $10^{-30} cm^6 s^{-1}$[42]. If we consider this value and the values presented in 10, for $\Delta n_0 \approx 10^{18}$, $R_r \gg R_A$, for $\Delta n_0 \approx 10^{20}$, $R_r \approx R_A$ and for $\Delta n_0 \approx 10^{22}$, $R_r \ll R_A$.
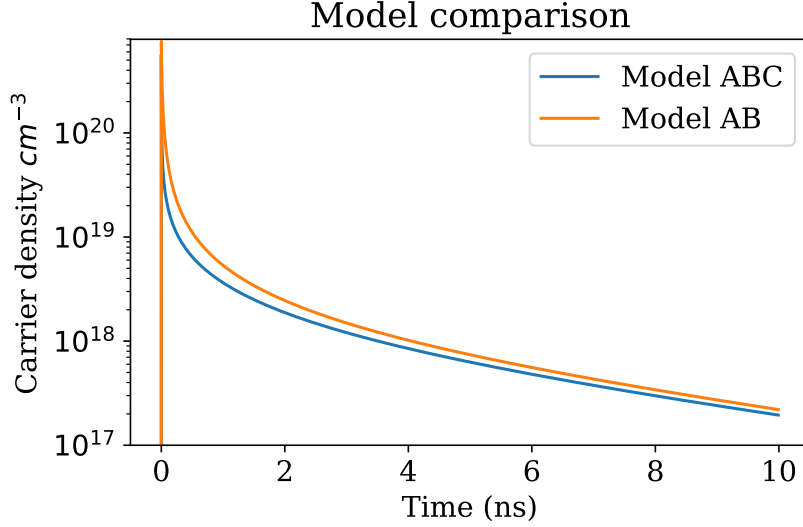
Figure 7: Numerical simulations of the ABC model with generation and recombination of carriers in intrinsic GaAs. Both the model including (blue) and excluding (orange) the Auger contribution are shown.

where the subscript i denotes the step (it runs from 0 to N, where N is the total number of steps) and Δt is the time difference between steps.

The simulation is divided into two time domains. For $i \in [0, 99]$, $\Delta t = 5 \cdot 10^{-15}$ s and G is given by a Gaussian curve with a full width half maximum of 250 fs and an amplitude of $G_0 = 4QP\lambda\alpha(\lambda)/(\pi d^2 \sigma_G hcR_{rep})$ (after equation 11). Here, $Q = 1$, $P = 2.5 \cdot 10^{-3} W$, $\lambda = 345 \cdot 10^{-9} m$, $\alpha = 7.17 \cdot 10^5 cm^{-1}$ [10], $d = 10^{-4} cm$, $\sigma_G = (250/2.335) \cdot 10^{-15} s$, $R_{rep} = 5.04 \cdot 10^6 Hz$ and h and c are Planck's constant and the speed of light respectively.

In the second time domain, where $i \in [100, N]$, with N = 100 000, the time difference is given by $\Delta t = 1 \cdot 10^{-13} s$. In this domain, there is no generation of carriers, $G = 0$. We consider that carriers are generated optically, but the same trends should apply for electron-induced carriers.

For τ, we use a value that has been observed before in GaAs, namely $\tau = 5.8 \cdot 10^{-9}$. [25, p. 58] Further parameters are $B = 1.7 \cdot 10^{-10} cm^3 s^{-1}$ and $C = 7 \cdot 10^{-30} cm^6 s^{-1}$. [24]

Figure 7 shows a comparison of numerical simulations both including and excluding the Auger contribution (ABC and AB models, respectively). We observe that the Auger contribution is only significant during the first nanosecond after excitation. The shape of the decay curve does not change a lot due to the Auger contribution.

Figure 8 shows the same numerical simulation, but on a much smaller time scale. Here, the shape due to the Gaussian excitation is more clearly visible. Because carriers already start recombining during the generation period, the peak for the full ABC model is not as high as that for the model that excludes the Auger contribution.

To see what the effect of excitation laser power has on the evolution of $n(t)$, we have run the simulation for four different laser powers. These simulations are shown in figure 9, which shows both the absolute values of $n(t)$ (left) and the normalized values (right). Increasing P
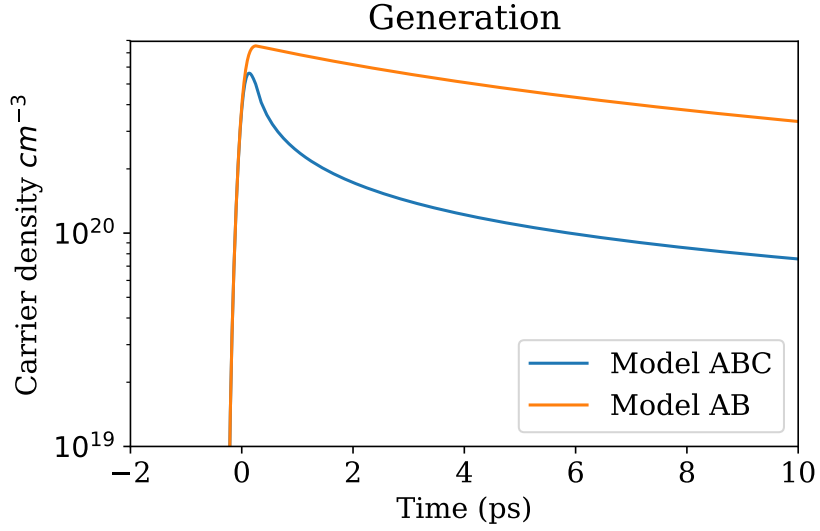
Figure 8: Numerical model of generation and recombination of carriers. The model is identical to that shown in figure 7, but it is on a much shorter time axis.

has the effect of decreasing the radiative lifetime (i.e. the initial peak gets narrower). The amplitude of the peak, compared to that of the tail also gets larger for increasing P.

As was already stated in section 2.3, the luminescent signal proportional to $n(t)^2$. When considering the luminescent signal, we also have to take into account that the measured signal is a convolution of the physical signal and the instrument response function. The latter can be well approximated by a Gaussian distribution, as will be discussed in section 3.4. Figure 10 shows an example of a physical signal, as calculated with the ABC-model (orange curve). It also shows the same signal, but convoluted with a Gaussian distribution characterized by $\sigma = 2.2 \cdot 10^{-11}\,s$ (blue curve). The latter curve has an arbitrary amplitude.
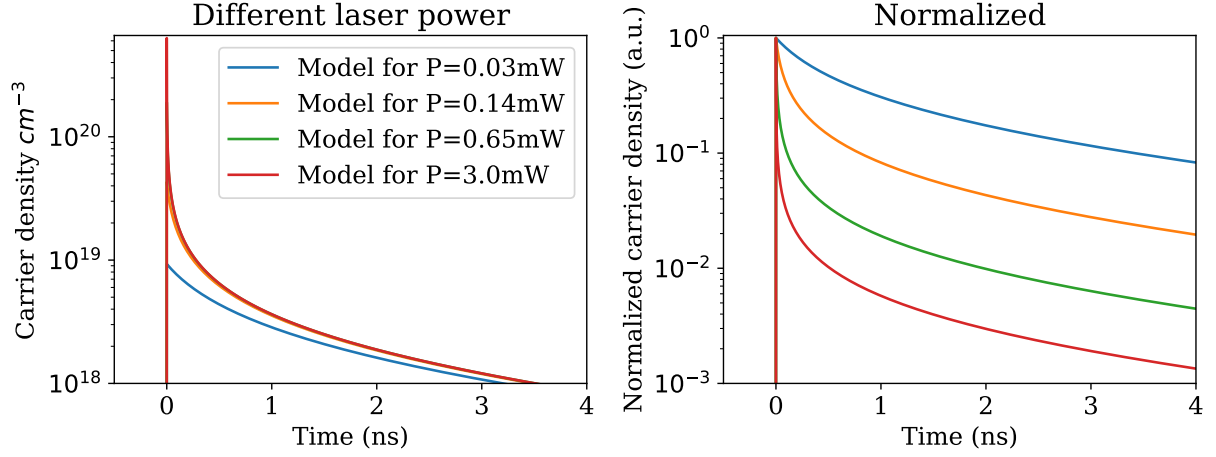
Figure 9: Comparison of numerically calculated decay curves due to different excitation laser powers, using the ABC model. The left figure shows the absolute values of n(t). Normalized curves are shown in the right figure to allow for better comparison.
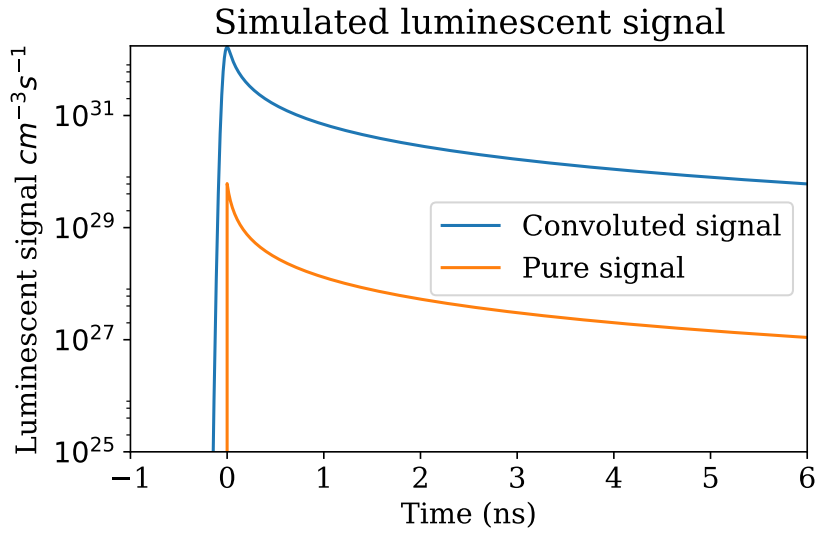

Figure 10: Comparison of a luminescent signal, as calculated with the full ABC-model (orange) and the same signal, but convoluted with a theoretical instrument response function. The blue curve has an arbitrary amplitude.

18

3   Experiment

To investigate the temporal evolution of the carrier density in a semiconductor after electron excitation, we need to excite the sample with short pulses of electrons. We make these pulses using a laser-driven pulsed scanning electron microscope (SEM). As was discussed in section 2, the semiconductor will start emitting photons after it is excited by this electron pulse. We can learn about the carrier dynamics that causes this luminescence by measuring the intensity of the light that is produced as a function of time (denoted by $S(t)$ in section 2). To do this, we use time-correlated photon counting measurements. As a comparative type of measurement, we also excite the semiconductor using a pulsed laser and measure the photoluminescence (PL).

3.1   Scanning electron microscope

We generate ultra-short electron pulses using a Thermo Fisher Quanta 250 SEM. The SEM has a Schottky field emission gun (FEG) with a tip (cathode) made from tungsten with a ZrO coating. This FEG can produce either a continuous current using thermionic emission, or a pulsed current by photoemission when it is driven by a laser. To generate a continuous emission of electrons, the tip is kept at a temperature of 1800 K with an extractor voltage of 4550 V. How we achieve the pulsed current is explained in sections 3.2.1 and 3.3.

3.1.1   Sample chamber

In both pulsed CL and PL experiments, the sample that we investigate is located in the vacuum chamber of the SEM. Light can go in and out of the chamber via a window, on the other side of which there is a collection of optical components. The layout of the sample chamber and the components directly outside of it is schematically shown in figure 11.
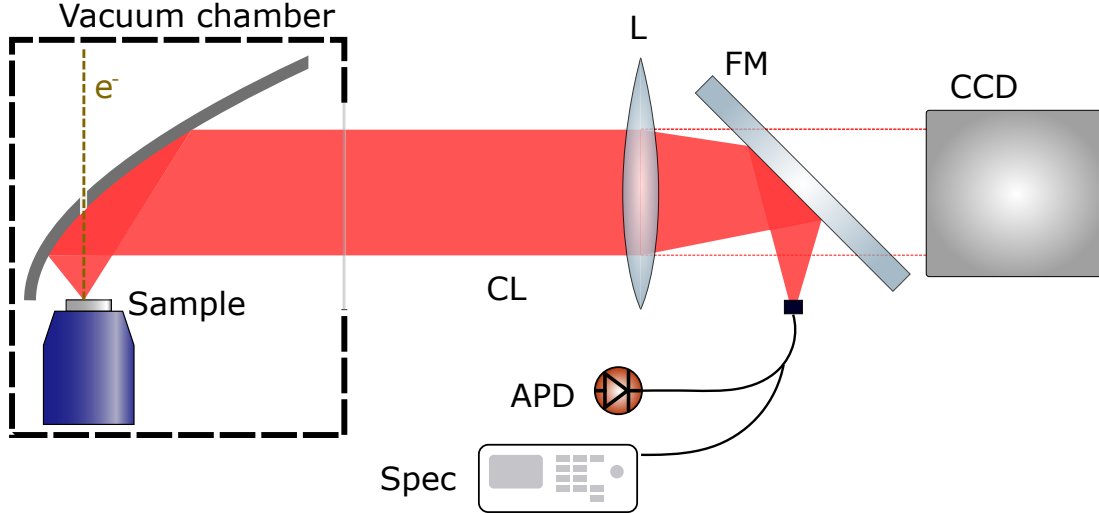
Figure 11: Schematic overview of the sample chamber and the optical components outside of it. The dashed yellow line represents the electron beam. The red sections represent the CL produced by the sample. This is focused onto a fiber which leads to either an avalanche photodiode (APD) or a spectrometer (Spec). The flip mirror (FM) and lens (L) can be removed to access the CCD camera with the CL.

In CL experiments, the electron beam passes through a hole in the mechanically controlled parabolic mirror, after which it is focused on the sample. The parabolic mirror is positioned such that its focal point is aligned with the area that is excited. We align the parabolic mirror by looking at the angular pattern of emission using a CCD camera (Princeton Pixis). [33, pp. 28-30] The CL of the sample is collimated by the parabolic mirror after which it passes through the window. Using a converging lens (L), the luminescence is focused onto an optical fiber which leads to either an avalanche photodiode (APD) for time-correlated measurements or to a spectrometer (Spec, Acton 2300i).

3.2   Optical setup

The optical setup that we use for our experiments is divided up into several subsystems. Figure 12 provides a schematic overview of the full optical setup. We use an Yb-doped fiber femtosecond laser (Clark MXR) that generates Gaussian pulses at a wavelength of 1034 nm (fundamental, red in figure 12) with a pulse duration of 250 fs at a repetition rate between 10 kHz to 25 MHz.[12] The fundamental is guided through a harmonic generator (HG). This generates a second harmonic (SH) beam at $\lambda = 517$ nm, a third harmonic (TH) beam at $\lambda = 345$ nm and a fourth harmonic (FH) beam at $\lambda = 258$ nm. The HG provides the flexibility to use several harmonics simultaneously. In appendix A, the harmonic generator is explained in more detail. In the following subsections (3.2.1 and 3.2.2), we will explain the remaining two optical subsystems.

---

[12]Though for our experiments, we only work at a repetition rates of either 5 MHz or 25 MHz.
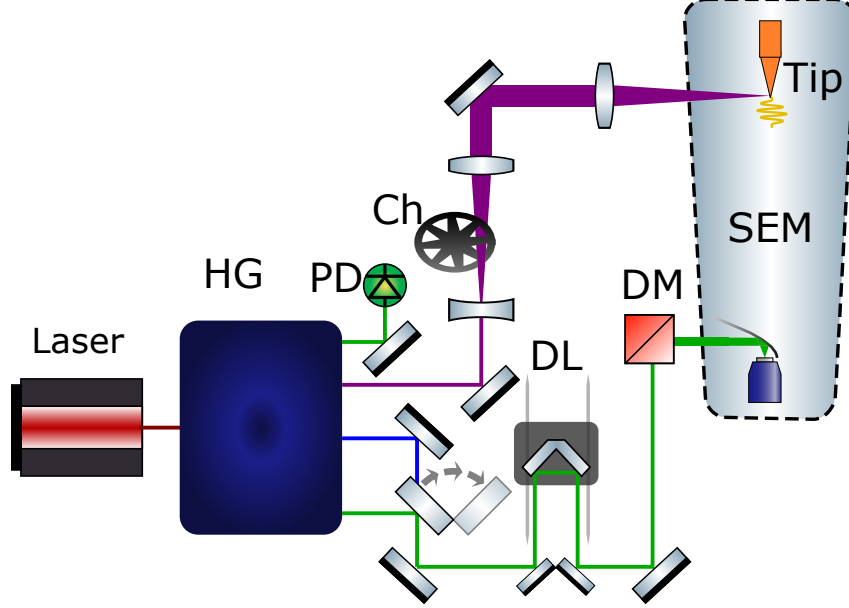
Figure 12: Schematic overview of our optical system (top view). The FH path (violet), modulated by a chopper (Ch) for lock-in measurements, is the path that is used for photoemission (see 3.2.1). The lower green line represents the SH/TH path used for PL experiments (see 3.2.2). It is guided through a delay line (DL) before it is directed to the sample chamber using a dichroic mirror (DM). The green line at the top represents the SH path that is sent to a photodiode (PD) to be used as a trigger for time resolved measurements (see 3.4). For a detailed explanation of the harmonic generator HG (in blue), see appendix A.

3.2.1   Photoemission path

To generate electron pulses for the cathodoluminescence experiments, the FH beam needs to be directed to the SEM. The violet path in figure 12 represents the FH beam path. After the FH beam is generated by the HG, it is guided towards two lenses in a telescope configuration using several mirrors. The telescope is used to increase the diameter of the beam. Located between these lenses, there is a mechanical chopper (Ch) which is needed for lock-in measurements.[13] The beam is finally guided towards the SEM using a periscope. How the FH beam is used to generate electron pulses is explained in section 3.3. Along the optical path, there are two mechanical mirrors which are controlled using a feedback system.[14]

3.2.2   Photoluminescence path

For photoluminescence measurements, we direct either the SH or the TH to the SEM chamber (where the sample is located). The beam path of the SH and TH beams is schematically shown in green in figure 12. Apart from the first mirror, both the SH and TH beams follow

---

[13]Lock-in measurements are explained in a bit more detail in section 3.3

[14]This feedback system (μAlinga) is needed because the optical table and the scanning electron microscope (which is driven by the FH pulses) are mounted on separate suspension systems. Without the feedback system, the beam path will easily become misaligned with the SEM system.

the same path. The excitation pulses are guided to a computer-controlled mechanical delay line (DL) using a set of mirrors. Similarly to the SEM path described above, there are two mechanical mirrors in the PL beam path which are controlled by a feedback system to make sure that the beam path will be well aligned to the SEM. A dichroic mirror (DM) is used to reflect the SH/TH beam into the SEM chamber. This part of the setup is schematically shown in figure 13. The parabolic mirror focuses the laser beam onto the sample and reflects the luminescence (red in figure 13) back out of the chamber. After passing through the DM, the PL is focused onto a fiber which guides it to either an APD or a spectrometer.
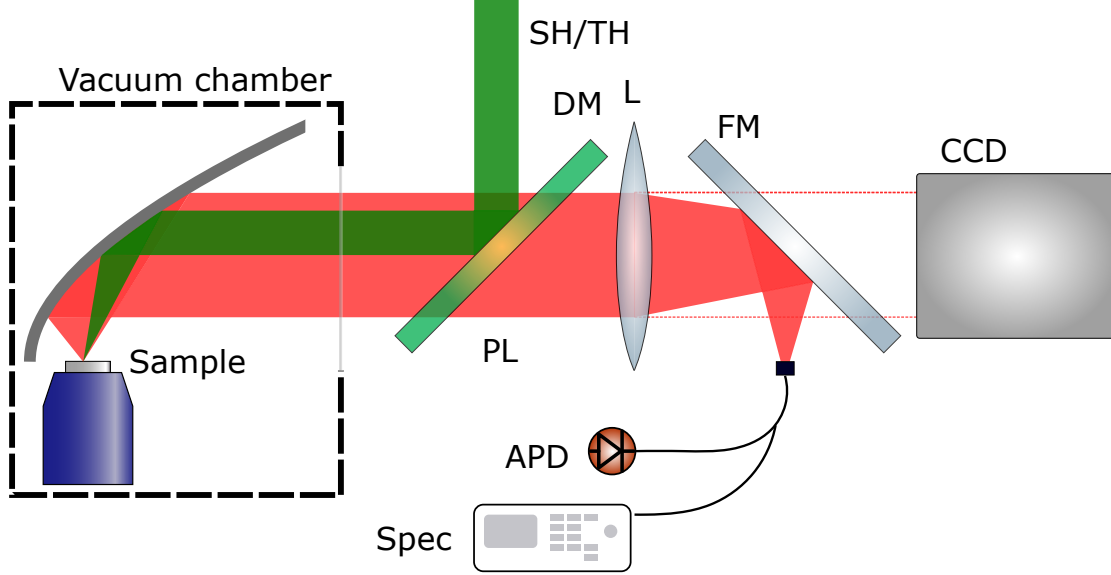

Figure 13: The same configuration as figure 11, but for PL experiments. The main difference with the configuration shown in figure 11 is that we added a dichroic mirror (DM). This reflects the laser (SH/TH, green) towards the chamber, but it lets the PL pass through to the lens.

3.3   Laser-driven pulsed SEM

To achieve a pulsed current, the SEM tip must be driven by our laser while thermionic emission is suppressed. The latter is achieved by lowering the temperature of the tip to 1200 K.[15] At this temperature, the work function of the tip is approximately 2.6 eV.[6, pp. 64-65] The photon energy of the light used to drive the SEM needs to exceed this value (equivalent to $\lambda = 477$ nm) and thus only the third and fourth harmonics can be used for this purpose. We access the tip with the FH using a UV-transparent window which is built into the SEM. The electron pulses are focused in the same was as the continuous electron beam.

Several parameters have an effect on the properties of the generated electron pulses. The parameters that influence these the most are extractor voltage, filament current and FH power on the tip. In our experiments, we work with a low extractor voltage (650 V) which allows

---

[15]This is done by lowering the filament current of the FEG from 2.3 A to 1.7 A.

us to achieve high currents (i.e. more electrons per pulse). Working with this low voltage goes at the expense of spatial resolution, which is in the range of 100 to 150 nm.[16] A major advantage of the laser-driven SEM method is creating very *short* pulses of electrons, around 1 ps.[17][7, p. 33] By varying the FH power, we can modulate the average number of electrons per pulse from less than 1 up to around 1200.

3.4   Time-correlated measurements

To measure the luminescence intensity as a function of time, we use time-correlated single photon counting (TCSPC) measurements. In this section, we will first focus on the theoretical principle behind TCSPC and then on how we apply the principle in our setup.

3.4.1   The principle of time-correlated single photon counting

The goal of doing TCSPC measurements is getting a time-dependent luminescence intensity profile. Two detectors are needed for this kind of measurement: a trigger and a stop detector. Each time the trigger is activated, a clock will start to run. This clock will stop when the stop detector is activated, or it will reset when the trigger is reactivated.
This process is schematically shown in figure 14. The clock runs in time intervals Δt_i and the
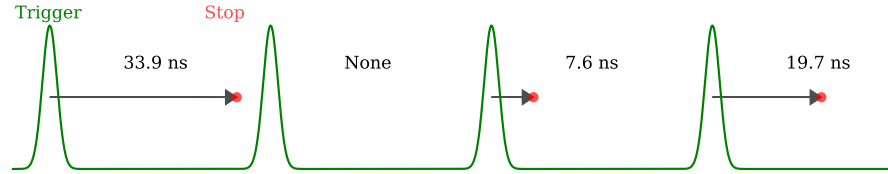

Figure 14: Schematic representation of the principle behind TCSPC. At each green peak (which represents the trigger), the clock is reset to 0. As soon as a fluorescence photon (in red) is detected, the clock stops and the time is recorded. If no fluorescence photon is detected, no time will be recorded.

time interval in which the stop detector is activated is recorded. A histogram of the recorded time intervals is made and this results in a so-called decay trace (see figure 15). [36, p. 2]

This type of measurement has an inherent bias due to the fact that *multiple* photons can arrive at the stop detector between two consecutive triggers. Only the first of these will be recorded into the histogram when this happens. This bias can be minimized by ensuring that the rate at which the trigger is activated is several orders of magnitude larger than that at which the stop detector is activated. [36, p. 3]

Another issue we encounter with this type of measurement is the inherent error in the time that a photon is detected due to the instrument response function (IRF). Figure 16 shows the IRF for our collection system (blue) and for CL measurements (orange). This issue means

---

[16]Other research groups have achieved resolutions down to 10 nm.[34]
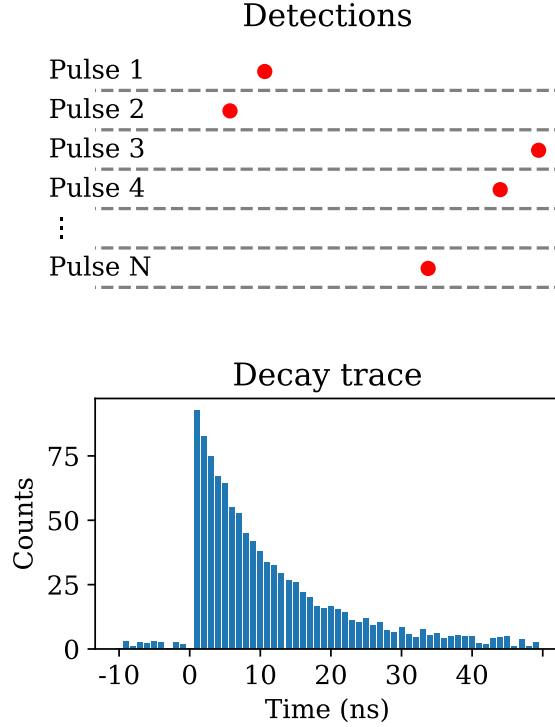[17]Other groups have even achieved temporal resolutions in the fs regime.[35]

Figure 15: An illustration of how a decay trace is made. The time bins (or interval) in which photons are detected are tallied in a histogram called a decay trace.

that the measured decay trace will be a convolution of the actual temporal luminescence profile and the IRF.

3.4.2 Time-correlated single photon counting setup

In the setup that we use for our time correlated measurements, the photodiode (PD) that we use as trigger is located directly outside of the harmonic generator. A second harmonic beam that is not used for excitation is directed towards this PD.[18] As is described in section 3.1.1, the luminescence (either CL or PL) is focused into an optical fiber. The fiber guides the luminescence to the time-correlation module where it first passes through an adjustable neutral density (ND) filter. After this, the luminescence path leads through a short pass 950 nm filter and a long pass 650 nm filter. Then it is measured by an avalanche photodiode (APD). Both the PD and the APD are connected to a correlator.

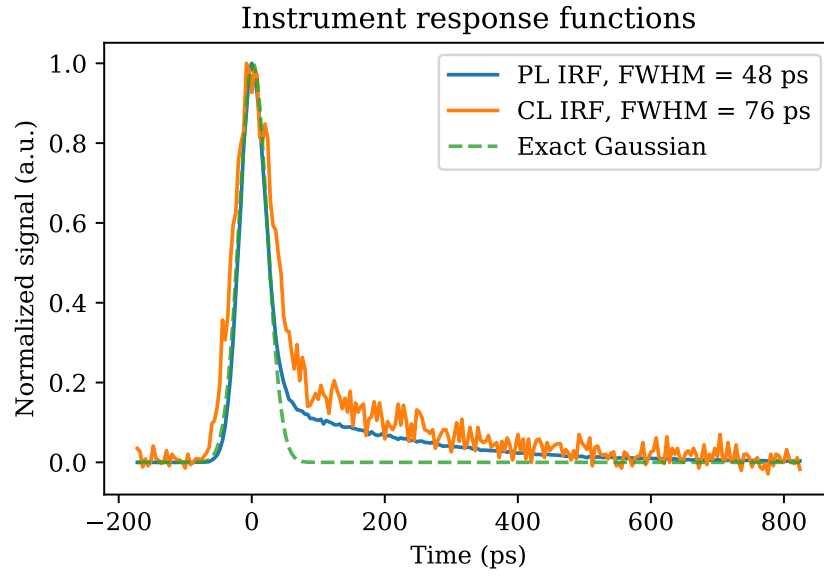[18]All harmonics generated by the HG are temporally correlated (see appendix A).

Figure 16: Instrument response functions of the time correlation system. The blue curve is measured by directly sending the SH to the APD. We used transition radiation (at 30 keV) of monocrystaline gold to measure the orange curve. The blue IRF is well approximated by the dashed green line, which is an exact Gaussian distribution.

4 Results

The main goal of this thesis is to study the fast electron-induced carrier dynamics in CZTS and GaAs. We also study optically induced carrier dynamics in these materials in order to have a reference for the fast electron-induced experiments. Several recombination processes occur during and after excitation by fast electrons or light. One of these processes is radiative recombination, where an electron and a hole recombine while emitting a photon. This means that the material will give of luminescence upon excitation. In the case of excitation by fast electrons, the emitted luminescence, either due to carrier recombination or other processes, is called *cathodoluminescence* (CL), and in the case of optical excitation, *photoluminescence* (PL). In this work, we study these types of luminescence extensively, in order to gain insight into the carrier dynamics in our samples. We do this in part by studying the luminescent spectra of the materials (see 4.1.1 and 4.2.1). The bulk of our results, however, is based on time-correlated single photon counting (TCSPC) measurements. These are analyzed qualitatively and quantitatively where possible, by using the ABC-model, which was presented in sections 2.2 and 2.4. Whenever we do PL experiments, we estimate the excitation spot to have a diameter of 10 μm. Generally, we use pulse energies of between $E_p = 10$ pJ and $E_p = 900$ pJ, these correspond to fluences of 0.012 and 1.1 $mJcm^{-2}$ respectively.

4.1 CZTS

The first sample that we will discuss the results of is Cu_2ZnSnS_4 (CZTS). CZTS is a direct band-gap semiconductor with a band-gap of between 1.4 and 1.6 eV. [2] The sample that we use in our experiments is polycrystalline CZTS on a glass substrate. It is also coated with a 3 nm thick layer of Al_2O_3. The sample was obtained from professor Xiaojing Hao's group, working at UNSW Sydney. For all experiments on the CZTS sample, we set the repetition rate of our laser to $R_{rep} = 25.19$ MHz.

4.1.1 Luminescent spectra

As a first step to investigate the recombination dynamics of CZTS, we have studied the behavior of the CL spectrum as a function of the number of electrons per pulse (N_e). As a comparative measurement, we have also measured the PL spectra as a function of laser pulse energy (E_p). Figure 17 shows both the CL and the PL spectra. The PL spectra shown in figure 17 (b) clearly exhibit a blue-shift with increasing laser pulse energy. To further investigate this trend, 18 (b) shows the peak wavelength as a function of the laser energy per pulse (blue data points). This effect has been observed before in CZTS and is attributed to the occupation of so-called tail states. [4] The saturation of the integrated PL signal, which can be seen in figures 17 (b) and 18 (a), has been observed in the same paper and is attributed to the same effect. [4] This saturation starts to become significant with laser pulses with an energy from around 200 pJ. After the saturation of the total PL signal, at around 500 pJ, we also observe a decrease in the total signal. This could be due to a misalignment between the laser beam and the parabolic mirror, causing a slight defocus of the laser pulses on the sample.
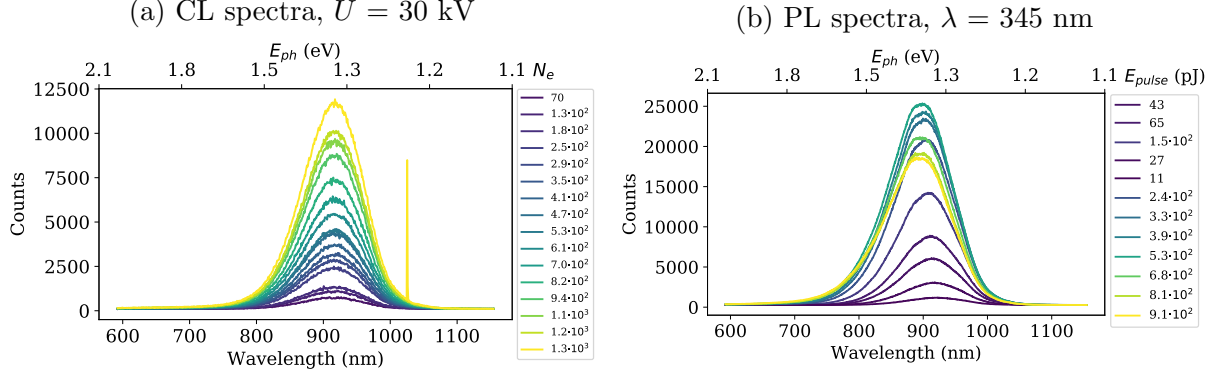
Figure 17: Luminescent spectra of CZTS for both CL (a) and PL (b). The wavelengths corresponding to the peak intensity and the integrated luminescent signal counts can be seen in figure 18.

The CL spectra of CZTS do not show a significant peak intensity shift, like the PL spectra do (see figure 18 (b)). This indicates that the saturation of tail states does not occur in the case of CL, at least in the regime of N_e that we have explored. Furthermore, the integrated CL count scales linearly with N_e (see figure 18 (a), green data points). We therefore assume that the initial excess carrier density Δn_0 scales linearly with the number of electrons per pulse N_e.
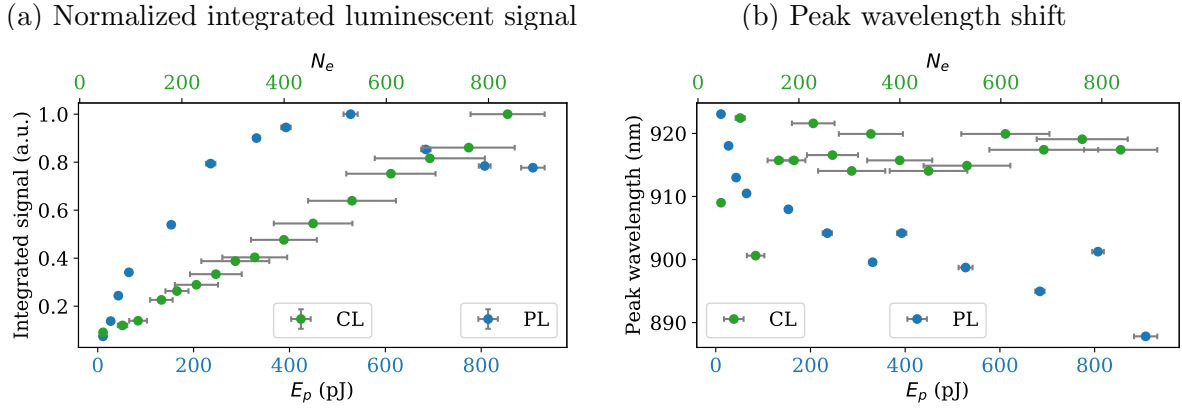

Figure 18: Integrated luminescent counts and peak wavelength shifts for CZTS, obtained with both CL (green) and PL (blue). The integrated CL count scales linearly with N_e, but the integrated PL count starts to saturate around 200 pJ to 300 pJ. For the CL spectra, the peak wavelength is not a function of N_e, but there is a blue-shift for the PL peak intensity.

4.1.2 CL decay traces

As was discussed in section 3.4, TCSPC measurements result in a so-called decay trace. A decay trace is a histogram of the total number of measured photons as a function of time. This measured signal will be a convolution of $B\Delta n(t)^2$ (see section 2.3) and the instrument response function (IRF).
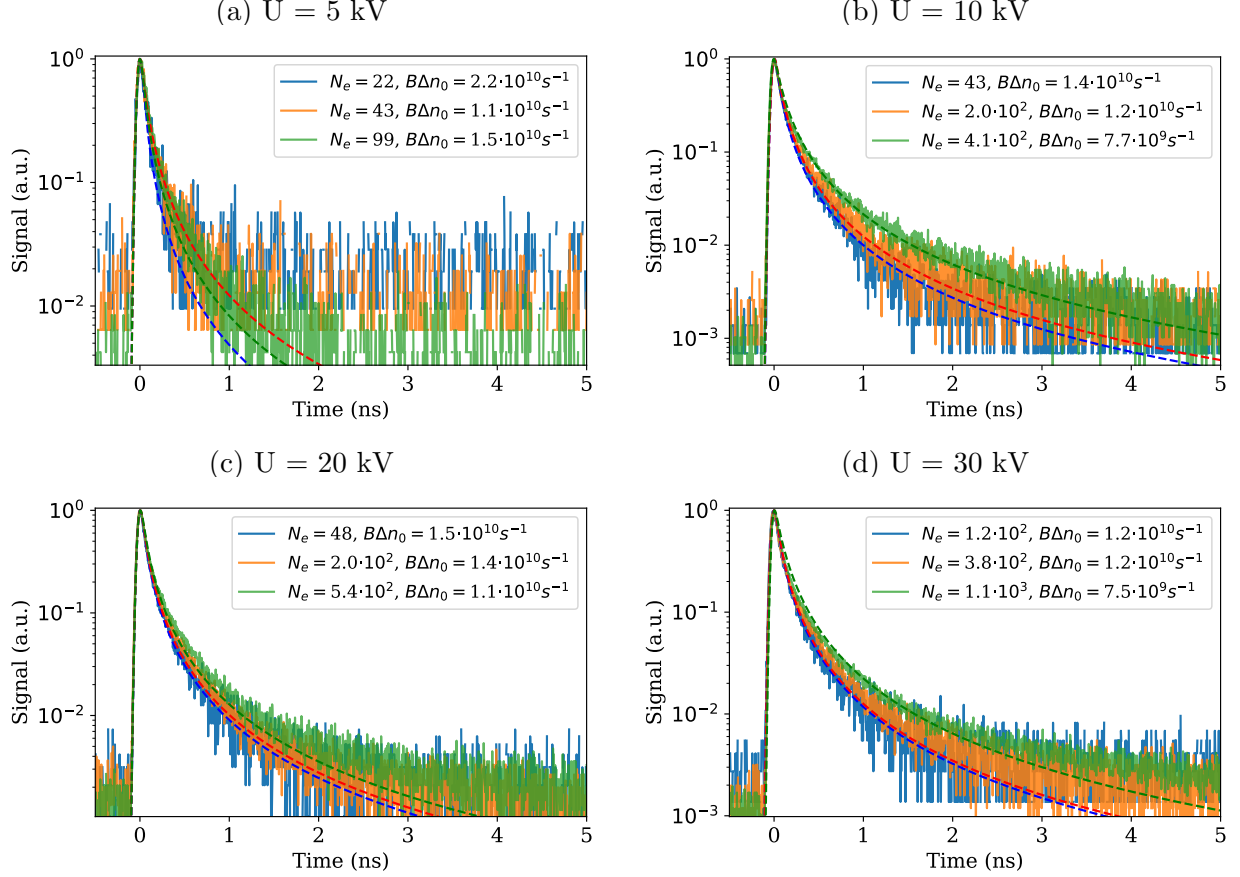
27

Figure 19: A selection of CL decay traces (solid lines) of CZTS with their associated fits (dashed lines). For each plot, the order of increasing current is from blue to orange to green. The 5 kV traces show no clear trend with increasing current, probably due to a low signal to noise ratio. In the other plots, we can see a clear trend of the luminescent lifetime increasing with increasing N_e. This indicates that the bimolecular coefficient decreases with increasing N_e (assuming that bimolecular recombination is the dominant recombination channel).

We have measured several sets of CL decay traces of CZTS at differing acceleration voltages: 5 kV, 10 kV, 20 kV and 30 kV. Within each of these sets of decay traces, we varied the N_e. Figure 19 shows a compilation of CL decay traces of CZTS. Each subfigure shows three decay traces at the same acceleration voltage, but with different N_e. The decay traces are normalized such that the peaks all align to the same value in order to make them easier to compare.

We have found that a convolution of equation 28 and a Gaussian curve provides a good fit function for the CZTS decay traces. This is because no purely exponential tail is observed at longer decay times, suggesting that SRH recombination does not play a major role. We also do not expect to achieve carrier densities for which Auger recombination will play a significant role, since the latter only typically does so for $\Delta n(t) > 10^{21}\,cm^{-3}$. [23] Our model therefore assumes bimolecular recombination to be the predominant process. The validity of this assumption is further confirmed by the fact that most fits yield a χ^2_{red} (goodness) of between 0.75 and 4 (which indicates that the model describes the physics reasonably well.

[37, p. 97])
These fits are represented by the dashed lines in figure 19. The fit function contains three fit parameters: the time shift t_0, the Gaussian variance σ_G (which accounts for the IRF) and the quantity $B\Delta n_0$. This last quantity is the product of the bimolecular coefficient and the initial excess carrier density Δn_0. We expect Δn_0 to scale with the N_e, like we discussed in section 4.1.1. Therefore, if we assume B to be constant, the radiative lifetime ($\tau_r = \Delta n/R_r$) should decrease with increasing current (see equation 28). This is, however, not what we observe in figure 19: the lifetime increases with increasing N_e for the 10 kV, 20 kV and 30 kV traces. The 5 kV traces do not show a clear trend, possibly due to the high noise level. At the end of this section, we will also present the differences between traces at roughly the same N_e but at different acceleration voltages.

As was stated before, we have fitted the decay traces with a convolution a Gaussian distribution and equation 28. The most relevant fit parameter in this fit function is $B\Delta n_0$, since this is the only quantity that is directly related to the carrier dynamics. Figure 20 shows the value of this quantity (orange dots) that corresponds to the best fit for all traces. The figure also shows the χ^2_{red} (blue dots) for each fit. It is hard to distinguish a trend in the 5 kV data, given that the data is evry noisy, as could already be seen in figure 19 (a). The 10 kV, 20 kV and 30 kV data, however, all show similar trends. We observe that the value of $B\Delta n_0$ first decreases with increasing N_e. Then, at around $N_e = 50$, it stabilizes at a value around $B\Delta n_0 \approx 1.4 \cdot 10^{10} s^{-1}$ with N_e. Finally, at several hundreds of electrons per pulse, the value again decreases as a function of N_e. These values are also consistent with the compilations of decay traces shown in figure 19.
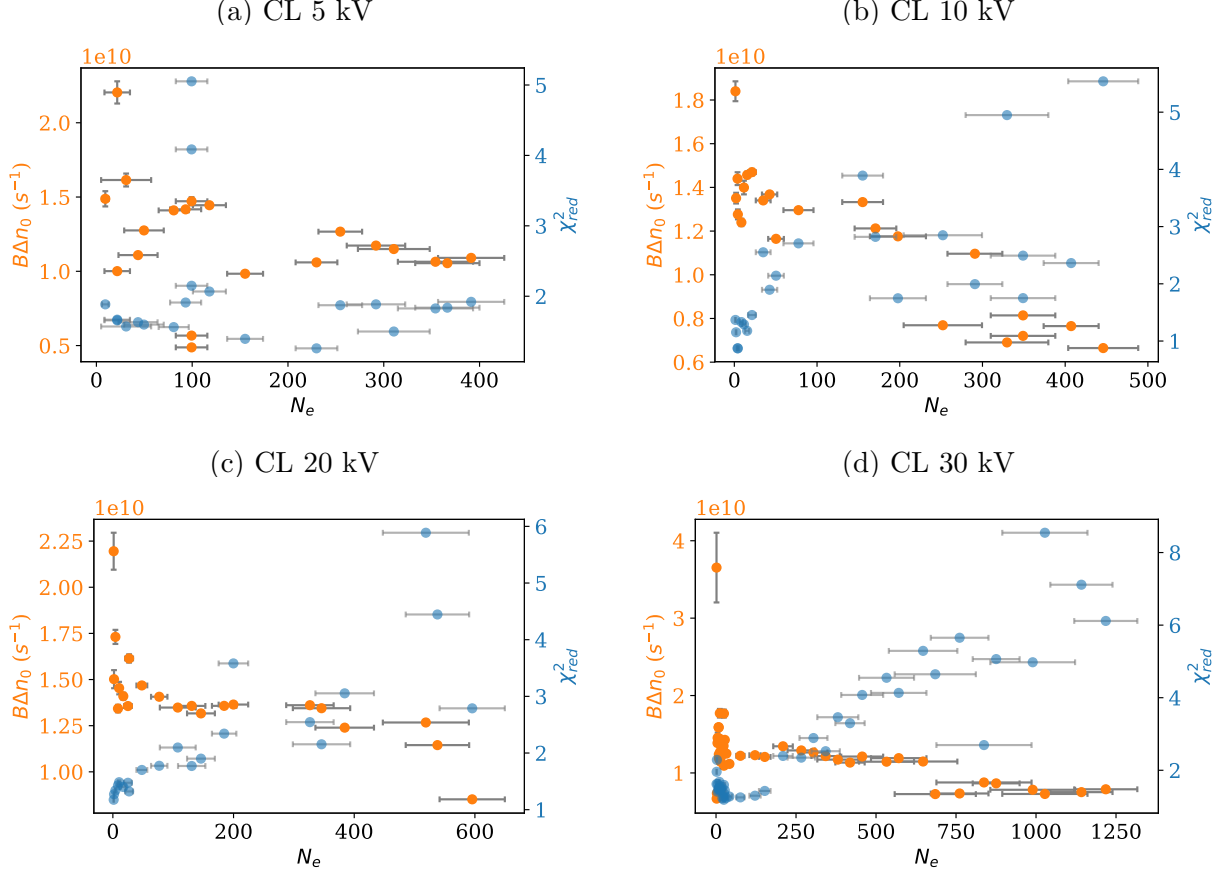
Figure 20: The fit parameter $B\Delta n_0$ as a function of the number of electrons per pulse and the associated χ^2_{red}. Larger values of $B\Delta n_0$ corresponds to shorter lifetimes. This means that the values shown here show a similar trend as could qualitatively be seen in figure 19. The 5 kV data does not show a clear trend, but the other plots do show similar trends. The values of $B\Delta n_0$ are high for low N_e, then they quickly decrease with increasing N_e before they stabilize. For very large N_e, a slight decrease is observed. The χ^2_{red} is between 1 and 5 for most fits, which indicates that the model that we use describes the underlying physics reasonably well.

It is remarkable that the value of $B\Delta n_0$ *decreases* with increasing N_e, since we expect Δn_0 to increase with increasing N_e. The results that are shown in figure 20 therefore indicate that the value of the bimolecular coefficient B is variable and decreases for increasing N_e. Using the CASINO simulations presented in section 2.1.2, we can make a rough estimate of the peak Δn_0 induced by an electron pulse. This Δn_0 can be estimated for a given acceleration voltage and number of electrons per pulse. For this, we assume that the peak carrier density scales linearly with the number of electrons. This is not an unreasonable assumption since the integrated CL signal also scales linearly with N_e (see figure 18 (a)). We estimated the peak Δn_0 using

$$\Delta n_0 = \frac{N_e \Phi_{max} Q}{E_g}. \tag{35}$$

Here, Q is the fraction of the energy that is used to generate e-h pairs and Φ_{max} is the peak

energy density[19] (which is given in table 2). Estimating Δn_0 allows us to calculate B as a function of N_e. We have used a value of $Q = 0.3$ for this calculation. Figure 21 shows these calculated values of B for four different acceleration voltages. For all cases, we find values for B of between $10^{-13} cm^3 s^{-1}$ and $10^{-8} cm^3 s^{-1}$. Typical values of B for direct band gap semiconductors are on the order of $10^{-10} cm^3 s^{-1}$. [23, p. 87] We observe a very clear trend which indicates a power law dependence for all acceleration voltages. It must be noted that the estimates for Δn_0 are quite rough, and the absolute values of the calculated B should not blindly be trusted. However, the absolute values should not affect the trend, so the trend that is shown in figure 21 likely can be trusted.
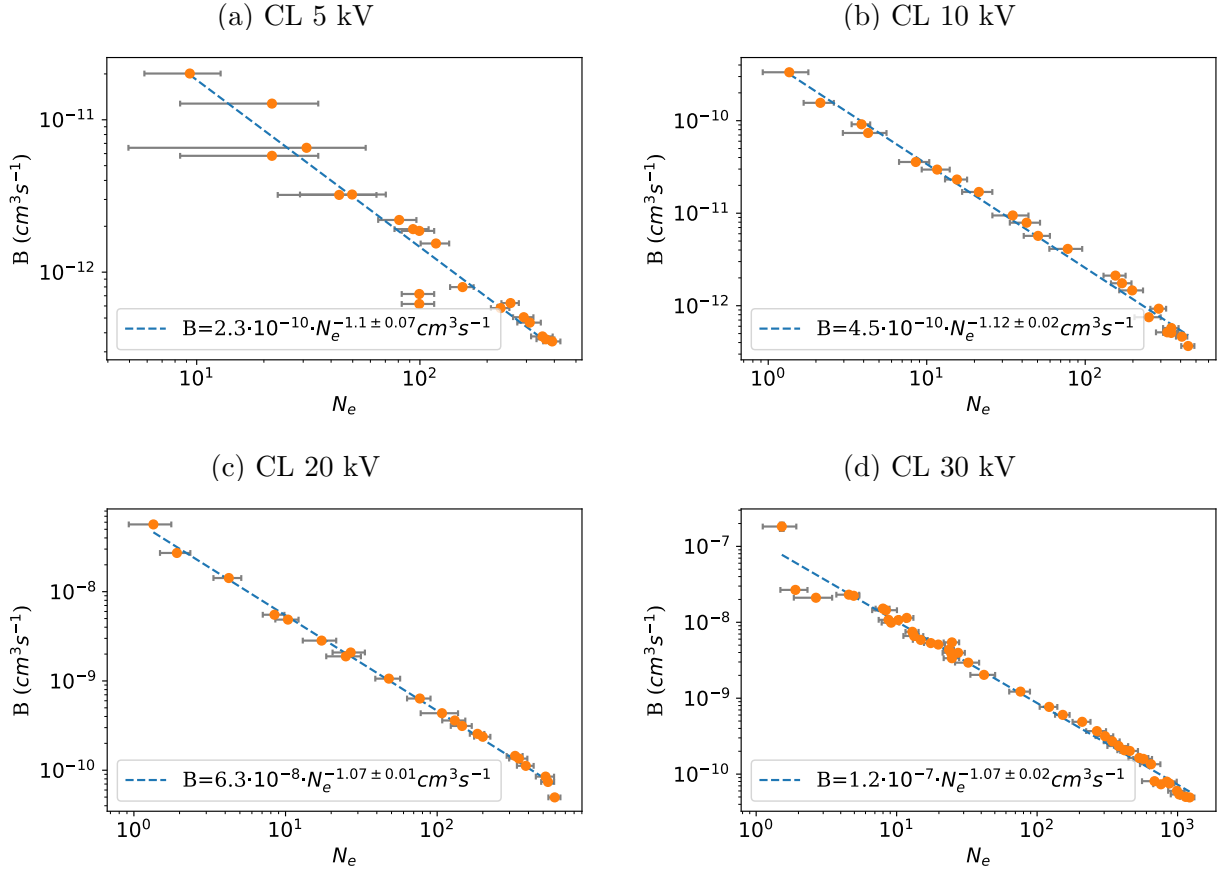

(a) CL 5 kV

(b) CL 10 kV

(c) CL 20 kV

(d) CL 30 kV

Figure 21: If we assume that the initial carrier density Δn_0 increases linearly with the number of electrons per pulse, we can calculate the N_e dependence of B. These calculated values (based on the values shown in figure 20) are shown here (orange dots). We have also fitted all four data sets with power laws, which are shown within the subfigures.

For all acceleration voltages, we roughly find that $B \propto N_e^{-1.1}$. This result is surprising, given that we would typically expected that the value of B does not depend on carrier density. One explanation for this trend could be Coulomb screening effects occurring within the material. In this case, the high density of carriers created by the electron pulse within a

---

[19]We take the *peak* energy density because this will give the most luminescent signal, which is due to the luminescent intensity scaling with $\Delta n(t)^2$.

relatively small volume would create a screening effect, such that carriers no longer feel a large density. A similar effect has been observed in quantum wells. [27] We should also note that we have assumed that only bimolecular recombination takes place. However, if any other process would participate in the recombination process, then its effects with be embedded in the B parameter. In any case, more research is still required, to verify this hypothesis.

So far, we have only directly compared decay traces as a function of N_e, but not as a function of U. Figure 22 contains two subfigures, each showing three traces at different acceleration voltages but at roughly the same N_e. If we consider the CASINO simulations shown in section 2.1.2 (and more specifically, figure 5), we might expect that the radiative lifetime should increase with increasing acceleration voltage. This is because the peak energy density due to an incoming electron, and therefore the peak initial carrier density, decreases with increasing voltage. The figure shows a different picture however: most traces overlap fairly well. Except for the 10 kV trace in figure 22 (a), which shows a longer lifetime.
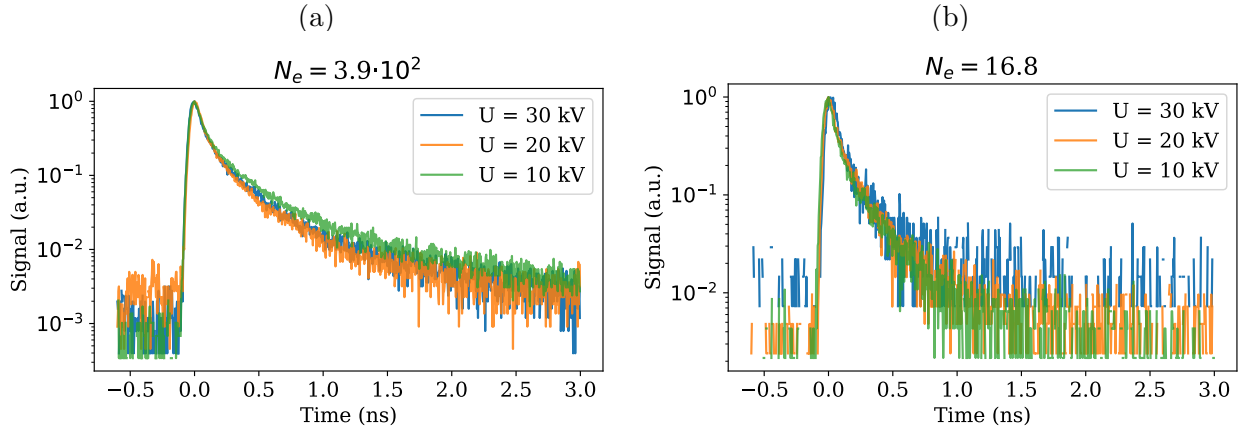

Figure 22: Each subplot shows three traces at different acceleration voltages, but at roughly the same number of electrons per pulse. All decay traces overlap well, except for the 10 kV decay trace in (a), due to its longer lifetime.

4.1.3   PL decay traces

Alongside the CL decay traces, we have measured two sets of PL decay traces of CZTS as a function of pulse energy E_p. For one set of traces, we used laser pulses at a wavelength of $\lambda = 345$ nm and for the other set, we used pulses at at wavelength of $\lambda = 517$ nm. A selection of the acquired PL decay traces is shown in figure 23, for both excitation wavelengths ((a) and (b)). The figure also shows the associated fits (dashed lines), for which we have again used a convolution of equation 28 and a Gaussian curve (so only considering bimolecular recombination). In this case, we observe a clear trend: the radiative lifetime becomes shorter with increasing pulse energies. This trend is in accordance with our expectations from equation 28, given that we expect $B\Delta n_0$ to scale with the laser pulse energy.
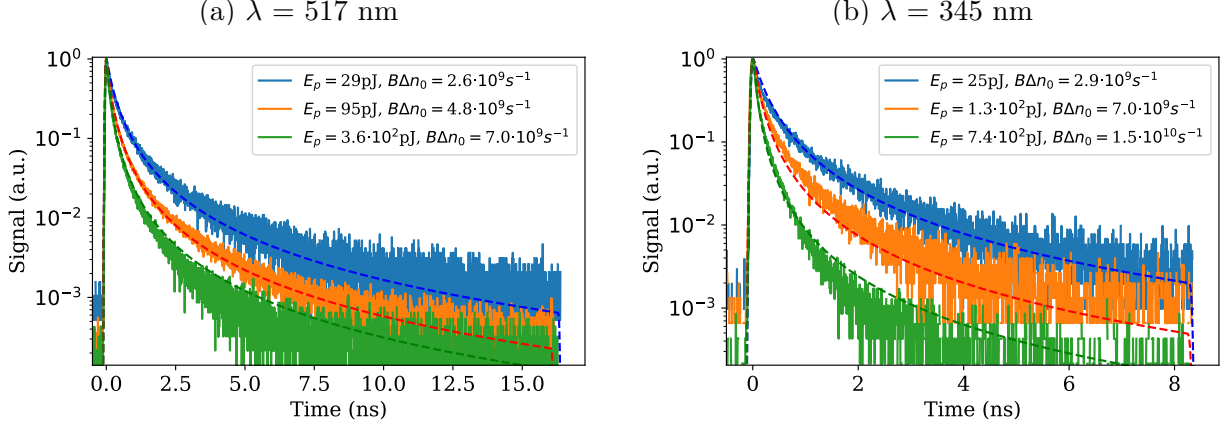
Figure 23: A selection of PL decay traces of CZTS (solid lines) and their associated fits (dashed lines). The difference between the separate plots is the wavelength of the laser pulses used for the excitation and the difference between the curves within a single plot is the pulse energy. For each plot, the order of increasing pulse energy is from blue to orange to green. As can be expected from equation 28, the luminescent lifetime decreases with increasing pulse energy.

As can be seen in table 1, the absorption coefficient of CZTS is the same for both wavelengths we use in our experiments. We therefore expect the initial excess carrier density not to be a strong function of excitation wavelength in the case of CZTS. The decay traces obtained with different excitation wavelengths but similar energy per pulse should therefore overlap. Figure 24 shows two comparisons of PL decay traces at the same pulse energy, but at different excitation wavelengths. It is clear that the traces overlap very well and this is an accordance with our expectations.
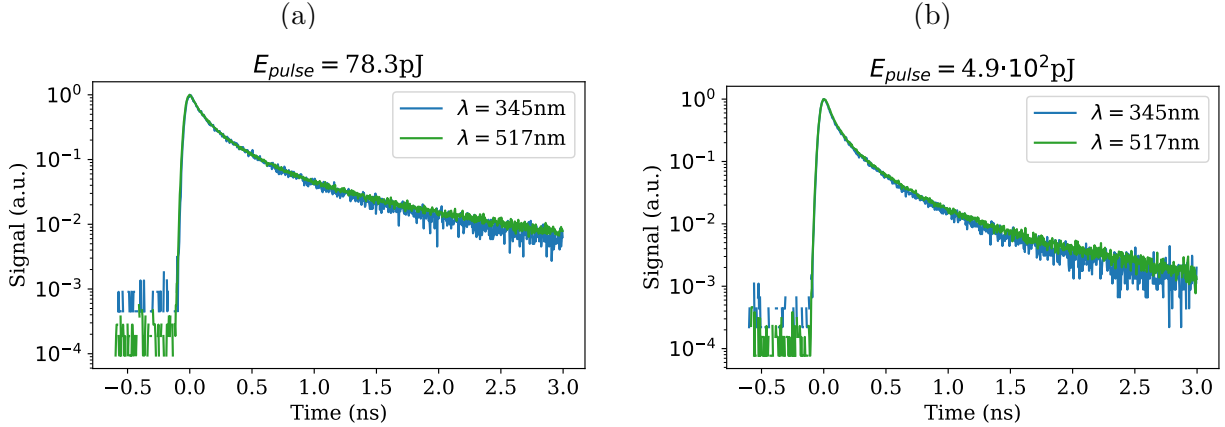

Figure 24: Comparisons of decay traces at different wavelengths but at roughly the same pulse energy. The traces show a strong overlap.

For a more quantitative analysis, we have determined $B\Delta n_0$ for all PL decay traces that we measured. If we assume B to be constant in the case of PL experiments, this quantity

33

should scale with the pulse energy E_p. We expect $B\Delta n_0$ to initially scale linearly with E_p, but when $E_p > 250$ pJ, it should follow a sublinear trend. This is because of the filling of the tail states that was described in section 4.1.1. Figure 25 shows $B\Delta n_0$ as a function of E_p for both sets of PL decay traces. We observe that $B\Delta n_0$ increases with the pulse energy, and it exhibits a linear increase up to approximately E_p 200 pJ, after which we observe a sublinear increase. Given that at low energies per pulse we expect a linear increase, we also fitted a straight line through all data points for which $E_p < 225$ pJ and $\chi_{red}^2 < 5$. The slope of this line can be used to determine B. For this we also need a value for Δn_0, which we approximate using an expression based on equation 7,

$$\Delta n_0 = \frac{\alpha E_p Q}{\pi r^2 E_g}.$$

(36)

Here, Q is the absorption efficiency[20] and r is the radius of the excitation spot. This expression corresponds to the peak Δn_0 (so just below the surface), since this will provide the most luminescence. Using this relation, with Q estimated to be 0.7, we determined the slope of the fit to correspond to $B = (4.8 \pm 0.2) \cdot 10^{-10} cm^3 s^{-1}$. This value is not surprising, since direct band gap semiconductors typically have B values on the order of $10^{-10} cm^3 s^{-1}$. There is a slight offset in the line which we attribute to a systematic error in the determination of E_p.
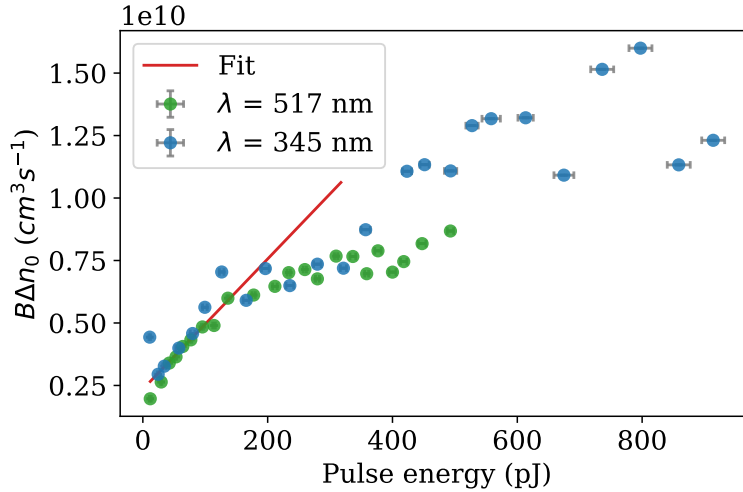

Figure 25: The fit parameter $B\Delta n_0$ as a function of the number of pulse energy. A straight line (red) is fitted through the seventeen data points for which $E_p < 225$ pJ and $\chi_{red}^2 < 5$. Larger values of $B\Delta n_0$ corresponds to shorter lifetimes. This means that the values shown here show a similar trend as could qualitatively be seen in figure 23.

4.1.4 Decay trace comparison

Finally, we will compare the traces of PL and CL experiments to each other. Figure 26 shows three examples of decay traces. One trace is from a CL experiment (orange) and the other

---

[20]Which, in this case, also accounts for the reflection at the surface.

two are from PL experiments. There is very little difference in shape between the decay traces. This indicates that the recombination mechanisms are very similar for all three cases.
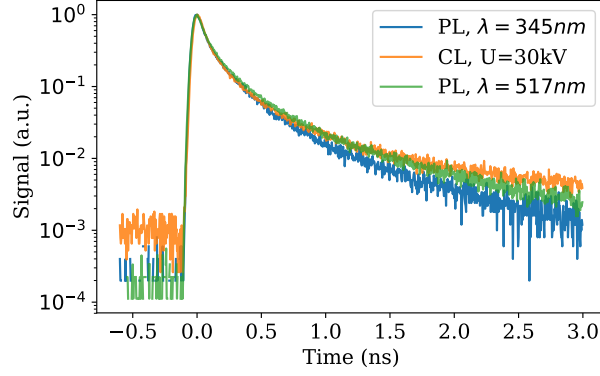

Figure 26: Comparison of three traces, each from a different set of measurements. The shape of the traces is roughly the same.

As we have already discussed, the main difference that we found between the CL and PL experiments is the dependence of B on N_e for CL, while it remains constant for PL.

4.2 GaAs

The next sample that we will discuss is GaAs. GaAs is a direct band gap semiconductor with a band gap energy of 1.43 eV (at 300 K). [8, pp. 190 - 205] The sample that we use in our experiments is bulk single crystal intrinsic GaAs with a thickness of 350 μm. For all experiments on the GaAs sample, we set the repetition rate of our laser to $R_{rep} = 5.04$ MHz.

4.2.1 Luminescence spectra

To start our analysis of the carrier dynamics in GaAs, we will look at the luminescent spectra. More specifically, we will look at the PL spectra as a function of laser pulse energy E_p. These spectra are shown in figure 27.
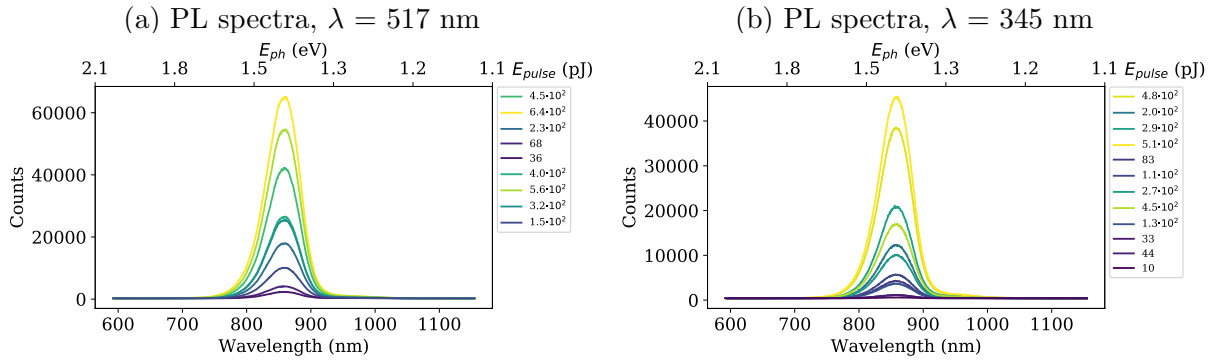

Figure 27: PL spectra of GaAs as a function of E_p for excitation wavelengths of (a) $\lambda = 517$ and (b) $\lambda = 345$.

The spectra show a predictable trend where the peak wavelength does not shift and the width of the spectra stays constant. Figure 28 shows the integrated luminescent signal and the wavelength at which the peak is located. Since the integrated signal scales linearly with E_p, we assume that Δn_0 does so as well.
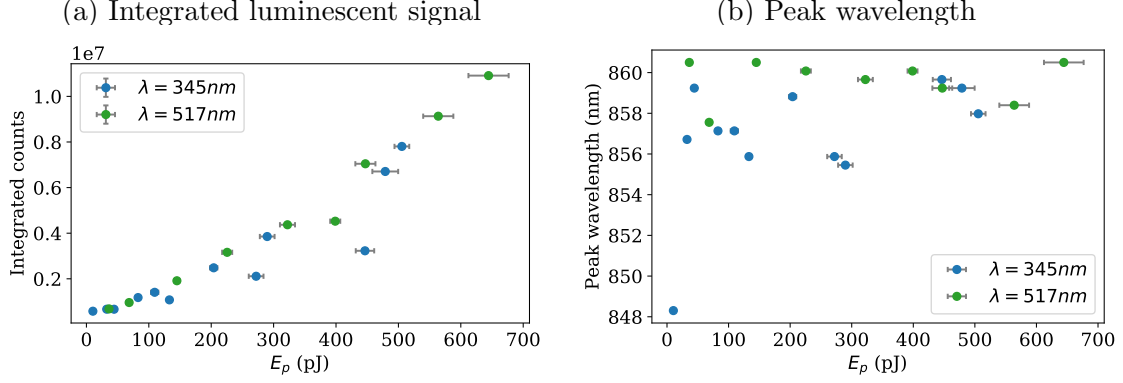
(a) Integrated luminescent signal   (b) Peak wavelength

Figure 28: Integrated PL signal (a) and peak wavelength (b) as a function of energy per pulse for laser excitation at $\lambda = 517$ nm and $\lambda = 345$ nm. The integrated luminescent signal scales roughly linearly with E_p for both wavelengths. The average peak wavelength of 860 nm corresponds to a photon energy of 1.44 eV, which is the same as the band gap energy of GaAs. [8, p. 190]

4.2.2 CL decay traces

We have measured two sets of CL decay traces of GaAs. One set was measured at an acceleration voltage of 10 kV and the other at 30 kV. Within each set, we varied the number of electrons per pulse, N_e, for each trace. Figure 29 shows a selection of CL decay traces for both acceleration voltages. Each selection is plotted on both a long (subfigures (a) and (c)) and a short time axis (subfigures (b) and (d)) to allow for a comparison of both the short and long timescales. All decay traces show a narrow peak width a temporal with of less than 0.5 ns, followed by a long exponential tail.
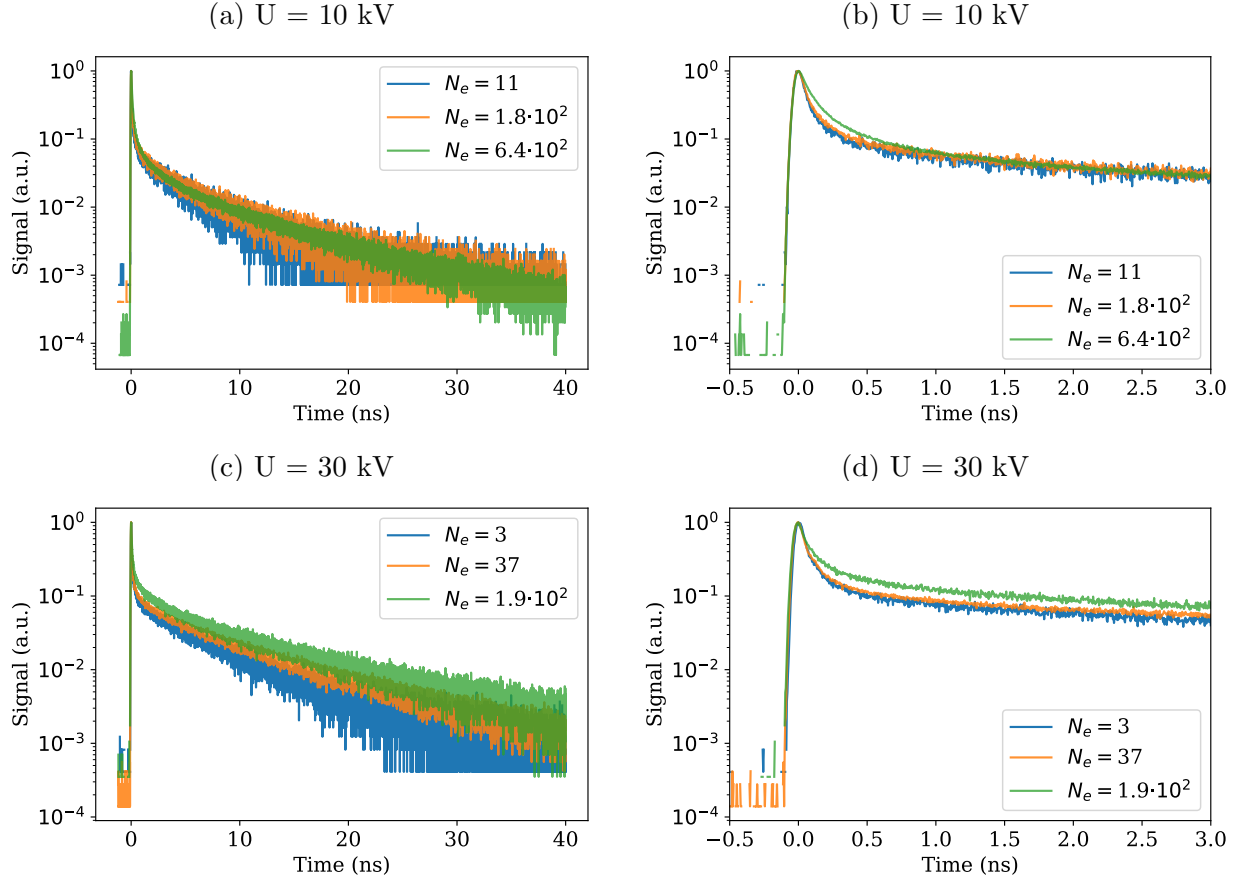
Figure 29: Selection of CL decay traces of GaAs. For each acceleration voltage, three traces are plotted on two different time axes. For each plot, the order of increasing N_e is from blue to orange to green. Plots (a) and (c) show a sharp peak followed by a long exponential tail. The slope of this tail decreases slightly with increasing current. Plots (b) and (d) clearly show that the sharp transition between peak and tail occurs before 0.5 ns and that the width of the peak increases with increasing current.

Figures 29 (b) and (d) show that increasing N_e has the effect of widening the peak at a short timescale (extending up to 0.5 ns). Subfigures (a) and (c) show that the lifetime corresponding to the exponential tail increases with increasing N_e.

It has not been possible to obtain a good fit with the model presented in section 2.3, as can be seen in figure 30. This figure shows two experimental CL decay traces, one at 10 kV and one at 30 kV ((a) and (b) respectively) Each subplot also contains three attempts of fitting the data with equation 31 for three values of $B\Delta n_0$, and a constant τ. As can be observed from the figures, we cannot fit the data with equation 31 for both short and long timescales: all solutions that show a good fit of the tail of the graph (long timescale) do not fit the peak at short times, and vice versa. This difficulty in fitting the data with equation 31 is attributed to the simplified origin of that equation. In this equation, carrier diffusion and surface recombination are not taken into account. These effects can however, lead to significant features in the experimental data.
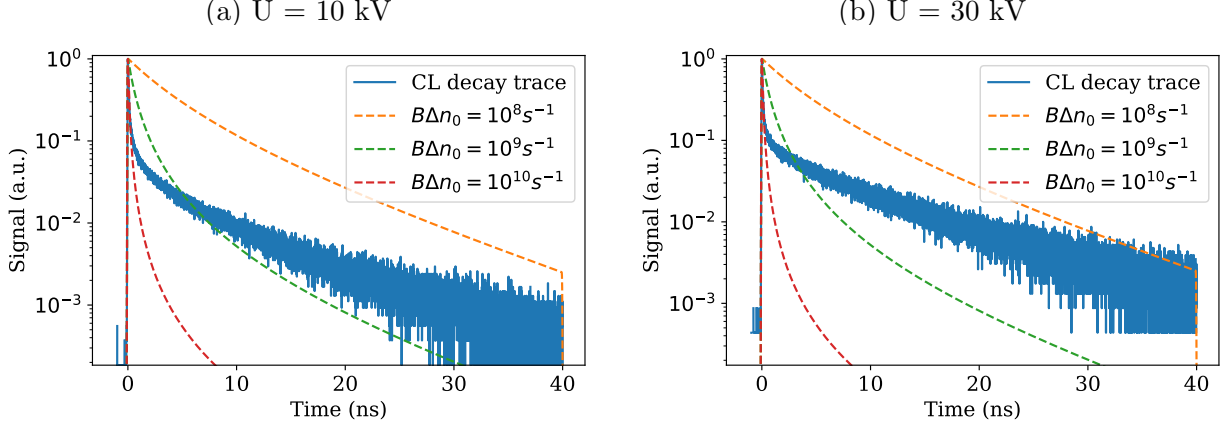
(a) U = 10 kV   (b) U = 30 kV

Figure 30: Two CL decay traces at different acceleration voltages, each plotted with three curves, obtained from equation 31 at three different values of $B\Delta n_0$. We use a value of $\tau = 20$ ns for each attempted fit. The equation clearly does not fit the decay traces well for any value of $B\Delta n_0$. Changing the value of τ also does not improve how well the curves fit the data.

Since we can not fit our model to these decay traces, we have fitted the traces using two exponential functions. The exponential that we use for the fast decay is convoluted with a Gaussian function to account for the IRF and is characterized by the time constant τ_{short}. Time constant τ_{long} characterizes the slow decay exponential fit (i.e. the tail). Even though fitting with two exponentials does not provide a perfect fit, it can give insights into the fast and slow recombination processes.

Figure 31 shows two examples of CL decay traces (the same as those in figure 30), one at 10 kV and one at 30 kV. Each decay trace is shown on both a long and a short time axis, along with their associated double exponential fits. The transition between the peak and the tail, typically between $t \in [0.5, 3]$ ns, is not reproduced well by the fit function. Outside these values for t, the fit function reproduces the decay trace rather well.
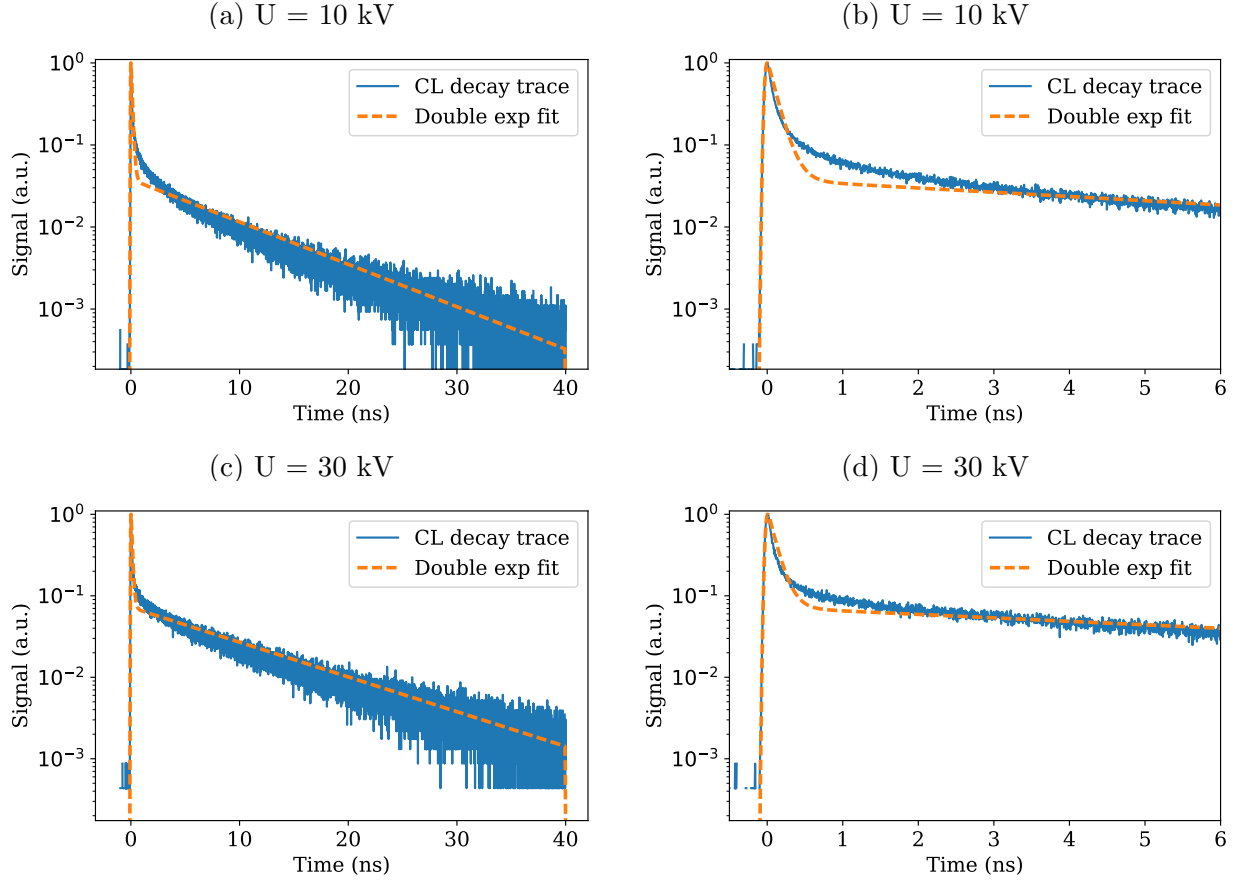
Figure 31: Examples of CL decay traces of GaAs at 10 kV, (a) and (b), and at 30 kV, (c) and (d). Each trace is plotted on two different time axes, along with their double exponential fit.

Figure 32 shows the fitted values of τ_{short} and τ_{long} (subfigures (a) and (b) respectively). Both the values of τ_{short} and τ_{long} for 10 kV (blue dots) are lower than those for 30 kV (green dots) at similar N_e. Values of τ_{short} scale linearly with N_e for both acceleration voltages. In subfigure (b), we observe that τ_{long} also scales with N_e, but the increase is not linear. The difference between the lifetimes of the U = 10 kV and U = 30 kV experiments will be further discussed in section 4.2.4.
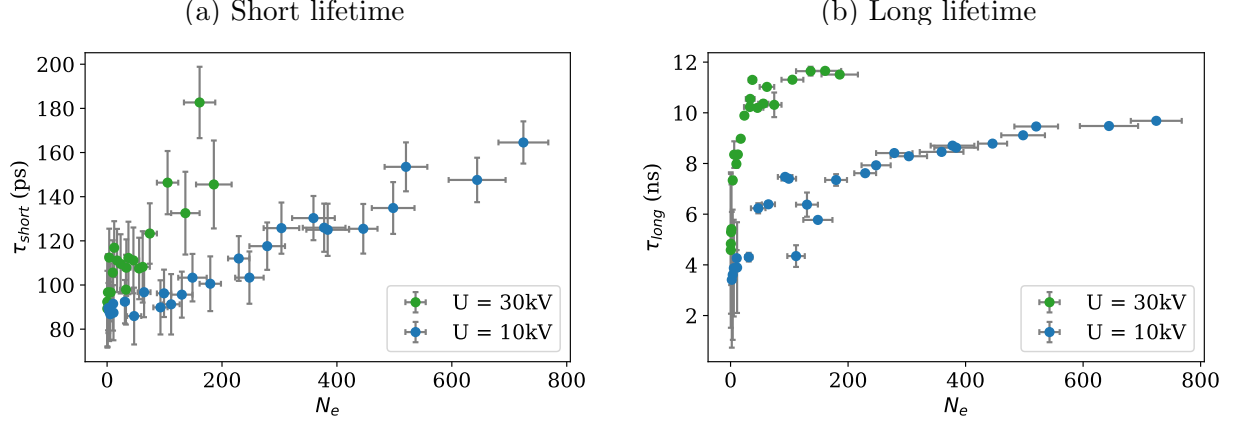
Figure 32: Short, (a), and long, (b), lifetimes of GaAs CL decay traces, obtained using two exponential functions.

The trend that we observe for τ_{long} in figure 32 (b) is remarkable. For low N_e, the lifetimes have a value of around 5 ns for both voltages. As N_e increases, the values of τ_{long} follow a roughly hyperbolic trend. The values corresponding to 30 kV stabilize at around $N_e \approx 150$, while the values corresponding to 10 kV do not stabilize in the regime of N_e for which we have measured.

Since the tails of the traces are well approximated by a simple exponential, we assume that they are caused by SRH recombination. If we consider equation 18, we expect the SRH lifetime not to change as a function of Δn for mid-gap traps. We do expect a τ that is variable in Δn if the traps are located either near the valence or the conduction band (i.e. deep traps). The value of τ should, however, go down for increasing Δn in this case. This would suggest that radiative recombination would remain the dominant type of recombination down to lower values of Δn as N_e increases, which is counter-intuitive.

A possible explanation for the trend that we observe in figure 32 (b) is that some type of trap saturation occurs at large N_e. This is an effect where recombination centers become occupied due to a high Δn, resulting in a longer recombination lifetime. [38, pp. 227-228] Similar trends to the one that we find in figure 32 (b) have been observed before in GaAs heterostructures. [39, p. 3] This would also explain the differences we observe between the 10 kV and the 30 kV data. The excitation volume in the case of 30 kV experiments is much larger than that in 10 kV experiments. This means that carriers will have to diffuse further to encounter unoccupied traps , when excited by 30 keV electrons. The saturation point is therefore reached earlier for 30 kV experiments.

4.2.3 PL decay traces

Similarly to our experiments on the CZTS sample, we have measured two sets of PL decay traces on GaAs. For one set, we used an excitation wavelength of $\lambda = 517$ nm, and for the other set, we used $\lambda = 345$ nm. A selection of PL decay traces at both excitation wavelengths is shown in figure 33. Just like in the case for the other figures showing GaAs decay traces, all traces are shown on both a long and a short time axis. Similar to the CL traces, all decay traces are characterized by a prominent peak, followed by a long exponential tail. The peaks

in the PL traces are temporally significantly wider than the peaks in the CL traces. This difference between PL and CL decay traces will be further analyzed in section 4.2.4.
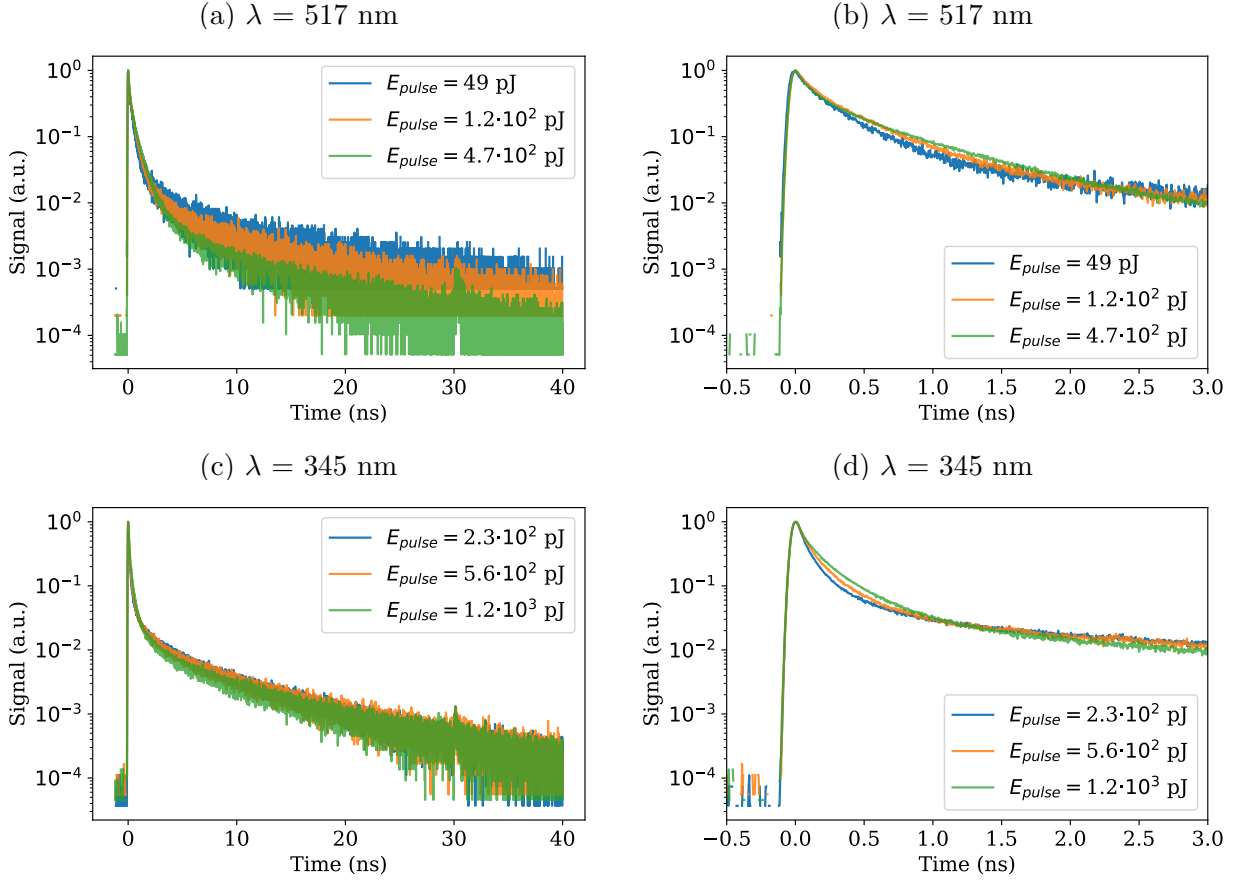

Figure 33: A selection of PL decay traces of GaAs. For each wavelength, two plots are shown of the same traces, but on different time axes. For each plot, the order of increasing pulse energy is from blue to orange to green. Plots (a) and (c) show a large peak followed by a long exponential tail. The slope of this tail decreases very slightly with increasing pulse energy. Plots (b) and (d) show that the width of the peak increases with increasing pulse energy.

Increasing E_p has the effect of making the fast decay (peak at short timescales) become longer and the transition from peak to tail becoming less sharp. It also has a slight effect on the lifetime of the exponential tail, which gets longer for larger values of E_p. Additionally, we observe that the ratio between the signal at short and long timescales increases with increasing E_p.

Like with the CL decay traces of GaAs, we have not been able to fit the PL traces with the model presented in 2.3. This is clearly visible in figure 34, which shows two decay traces (one at $\lambda = 517$ nm, (a) and one at $\lambda = 345$ nm, (b)), together with 3 curves in each cases, obtained with equation 31 at three different values of $B\Delta n_0$ (dashed lines). Especially the sharp transition from the peak to the exponential tail can not be reproduced with this function.
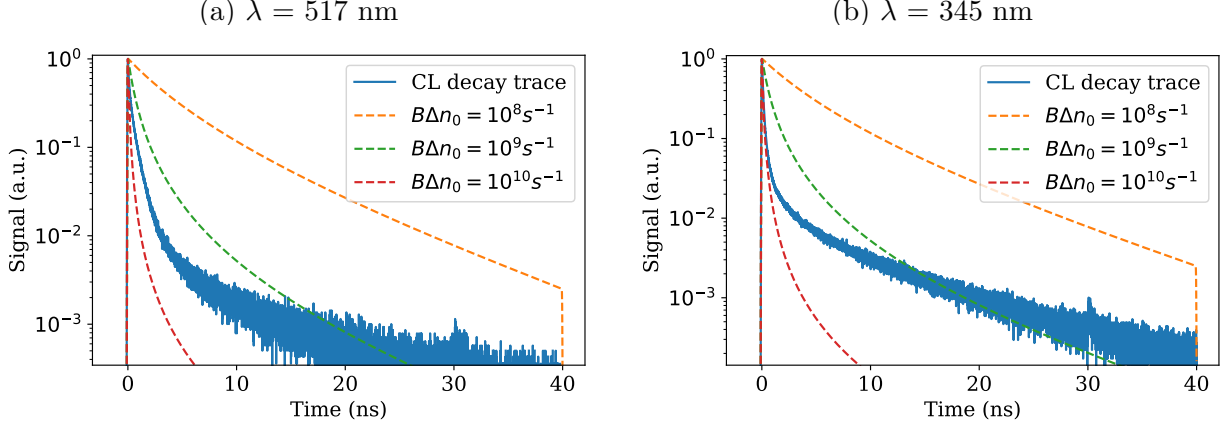
(a) $\lambda = 517$ nm

(b) $\lambda = 345$ nm

Figure 34: PL decay traces excited with $\lambda = 517$ nm, (a) and at $\lambda = 345$ nm, (b). The traces are plotted together with three curves obtained using equation 31 at three different values of $B\Delta n_0$ (dashed lines). It is clear that the dashed lines do not overlap well with the decay traces.

For this reason, we have fitted the PL decay traces with two exponential functions, just like we have with the CL traces. Figure 35 shows two examples of these double exponential fits.
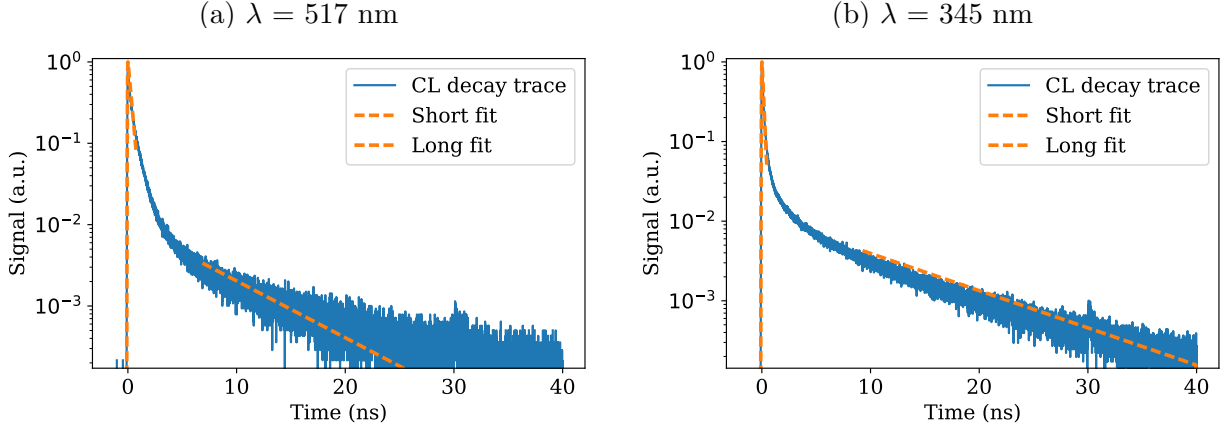

(a) $\lambda = 517$ nm

(b) $\lambda = 345$ nm

Figure 35: PL decay traces (blue) fitted with two exponential functions (orange).

We show the values of τ_{short} and τ_{long} as a function of E_p in figure 36. For both excitation wavelengths, τ_{long} initially increases with increasing E_p, before it stabilizes for $E_p > 200$ pJ. The short lifetime of the $\lambda = 517$ nm traces, green dots in figure 36 (a), scales with E_p for $E_p < 200$ pJ, before it stabilizes to a value of 280 ps. Then, τ_{short} decreases slightly with increasing E_p. For the $\lambda = 345$ nm decay traces, we only observe an increase in τ_{short} for increasing E_p.
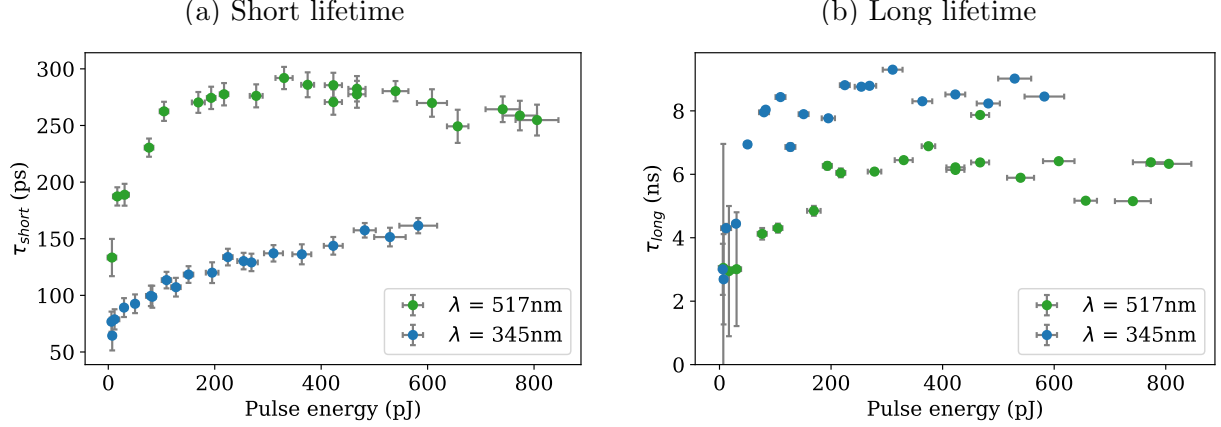
Figure 36: Short and long lifetimes ((a) and (b) respectively) of GaAs PL decay traces at λ = 517 nm (green dots) and at λ = 345 nm (blue dots).

We theorize that the initial increase and subsequent stabilization of τ_{long} is due to trap saturation. This is because the trend is very similar to the one that we see for CL experiments (see figure 32 (b)).

The increase of τ_{short} can be explained by considering a process called super-diffusion. In this process, the diffusivity D of carriers in a semiconductor exceeds the room temperature value D_0 by several orders of magnitude for a short period after laser excitation. [40] For silicon, it has been shown that the diffusivity, during the first 200 ps, increases by two to three orders of magnitude. This initial diffusivity is also shown to scale with laser fluence, meaning that the diffusion length $L_D = \sqrt{D\tau}$ also scales with laser fluence. If we assume that a similar effect occurs in GaAs, the diffusion length will be between 3 μm and 25 μm, depending on E_p.[21] Compare this to the diffusion length assuming no super-diffusion occurs: $L_{D,0} \approx 0.6\mu m$.

The increase in L_D will result in the carriers distributing themselves over a much larger volume. Even though the total number of excess carriers $\int \Delta n d\mathbf{r}$ scales linearly with E_p, the carrier density will decrease with increasing E_p due to the volume scaling superlinearly with this quantity. The smaller value of Δn results in a larger τ_{short}.

In figure 32 (a), we observe that τ_{short} for CL experiments scales with N_e. This trend is therefore somewhat similar to the one that we observe in 36 (a). Due to this similarity, we believe that the effects underlying these trends might be very similar as well. In other words, the scaling of τ_{short} with N_e in the case of CL might also be due to super-diffusion of carriers. More research would still be needed however, to confirm this hypothesis.

4.2.4 Decay trace comparison

Lastly, we will compare decay traces of different sets of measurements to each other. While we have found a strong overlap between CL and PL decay traces for CZTS, we do not find such an overlap between the CL and PL traces of GaAs. This can easily be seen in figure 37, which shows examples of decay traces of both CL (orange), and PL (blue and green) on two

---

[21]Assuming a room temperature diffusivity of $D_0 = 20cm^2s^{-1}$ [41] and a lifetime of $\tau \approx 200ps$.

different time axes. The most prominent difference between the CL and PL decay traces is the size and shape of the initial peak. This CL peak is very narrow and low compared to the exponential tail, whereas the PL peaks are wide and high compared to the exponential tail. The exponential tail itself does not differ much between CL and PL, aside from the onset. Since the tails of the CL and PL traces are roughly the same, we assume that they have the same physical origin, namely SRH recombination from the same type of traps. The peaks in the decay traces are caused by faster recombination processes and are caused by either mainly radiative recombination, or by a combination of Auger and radiative recombination.
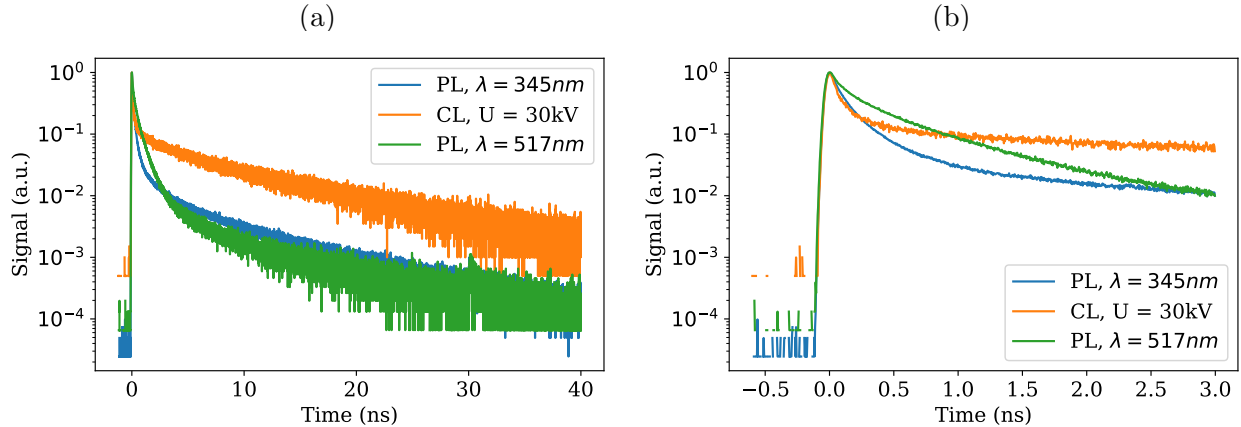

Figure 37: Comparison of a CL decay trace and two PL decay traces of GaAs. The orange curve corresponds to the CL 30 kV decay trace, and the blue and green curves correspond to the $\lambda = 345$ nm and $\lambda = 517$ nm PL traces respectively.

We believe that the sharp transition from the peak to the tail of the traces is caused by a combination of diffusion of carriers and surface recombination. Carriers are typically excited within 1 μm below the surface (see section 2.1), and consequently, this is where the highest carrier concentration will be. The high concentration of carriers causes strong luminescence as the carriers recombine, resulting in the sharp peak in the decay traces. At the same time, the carriers will diffuse, and the carriers that diffuse toward the surface will recombine there through dangling bonds. This surface recombination does not cause luminescence, but it does rapidly decrease the carrier concentration, i.e. it acts a a sink for the carriers. After the carrier concentration has dropped by enough, SRH recombination will become the predominant mode of recombination, causing a relatively sharp transition from the peak to the tail.

In CL experiments, we only excite carriers in a relatively small volume compared to PL experiments. The spatial gradient in carrier density is thus larger for CL experiments. We therefore expect diffusion to play a much more dominant role in the case of CL experiments. This results in the transition between the peak and the tail to occur much sooner and to be much sharper for CL decay traces compared to PL traces, as the carriers diffuse to the surface more quickly. We can easily observe this difference in figure 37 (b).

Figure 38 shows a comparison of CL decay traces at the same N_e but at different acceleration voltages. The difference between the 10 kV and 30 kV CL decay traces is mainly seen in the size and the duration of the peak. From the CASINO simulations that we presented in

section 2.1.2, we expect the carrier density due to 10 keV electrons to be significantly larger than that induced by 30 keV electrons. Such a difference in the carrier density should result in a shorter τ_{short} for the 10 kV decay trace (i.e. a narrower peak). This can not easily be seen in figure 38 (b), but it can be seen in figure 32 (a). A higher carrier concentration should also result in SRH recombination to become the dominant recombination channel at a longer delay. This results in the transition from the peak to the tail to occur at a later time for the 10 kV decay trace in figure 38 (b). This last feature could however also be explained if super-diffusion occurs, since this effect is dependent on the speed distribution of carriers. [40] It is conceivable that this speed distribution shifts to larger speeds when a larger U is used. This would result in the excitation volume to become much larger in the case of 30 kV compared to the case of 10 kV and the transition from peak to tail occurring sooner.
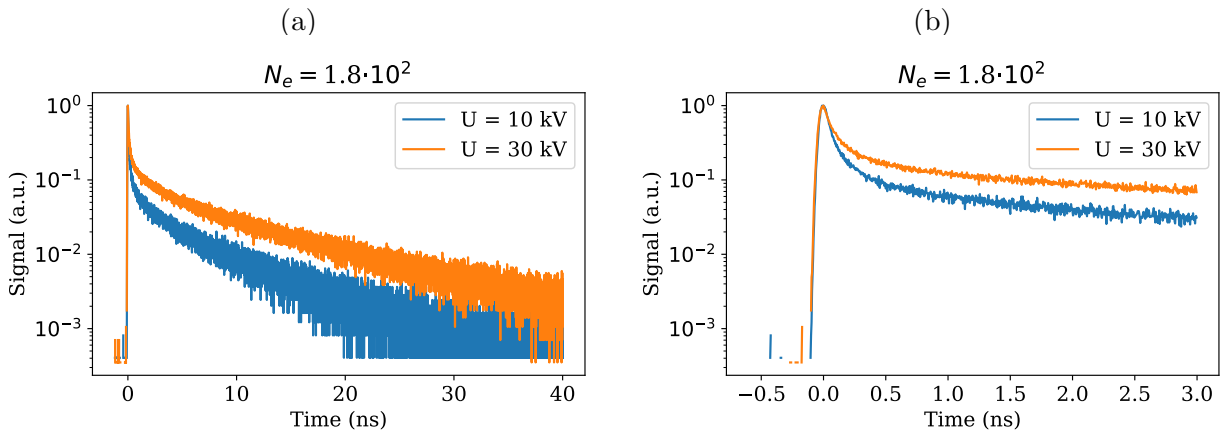

Figure 38: Comparison of GaAs CL decay traces at roughly the same N_e but at different acceleration voltages. The shapes of the exponential tails are very similar, but the relative size of the peaks is quite different between the traces.

We expect two main differences between PL experiments at $\lambda = 345$ nm and at $\lambda = 517$ nm if we use the same laser pulse energy E_p. The first is the penetration depth of the laser pulse and therefore the excitation volume. We expect the penetration depth (and excitation volume) for $\lambda = 345$ nm to be much smaller than that for $\lambda = 517$ nm, due to the difference in absorption coefficient of GaAs for these wavelengths (see table 1). The second difference that we expect is the peak carrier concentration. This difference is a result of the smaller excitation volume. Roughly the same optical energy is absorbed by a smaller volume for $\lambda = 345$ nm pulses, resulting in a larger peak carrier concentration.

Figure 39 shows a comparison of two PL decay traces where these differences should apply. Both decay traces were produced with approximately the same E_p, but at different excitation wavelengths. We observe a clear difference in the duration of the peak: the one that corresponds to $\lambda = 517$ nm (green) is much wider than that corresponding to $\lambda = 345$ nm. We ascribe this difference to the difference in carrier concentration. The latter is much higher for $\lambda = 345$ nm, resulting in a shorter radiative lifetime (see section 2.2.2).

The second difference that we observe between the decay traces shown in figure 39 (a) is the onset of the exponential tail. This onset occurs at a longer time for the $\lambda = 517$ nm trace. We believe that this is due to the diffusion of carriers and surface recombination. Since the

carriers are concentrated much more closely to the surface in $\lambda = 345$ nm experiments, their average distance that they have to cross to the surface, where rapid recombination occurs, is much smaller. This results in SRH recombination to become dominant sooner for $\lambda = 345$ nm than for $\lambda = 517$ nm experiments.
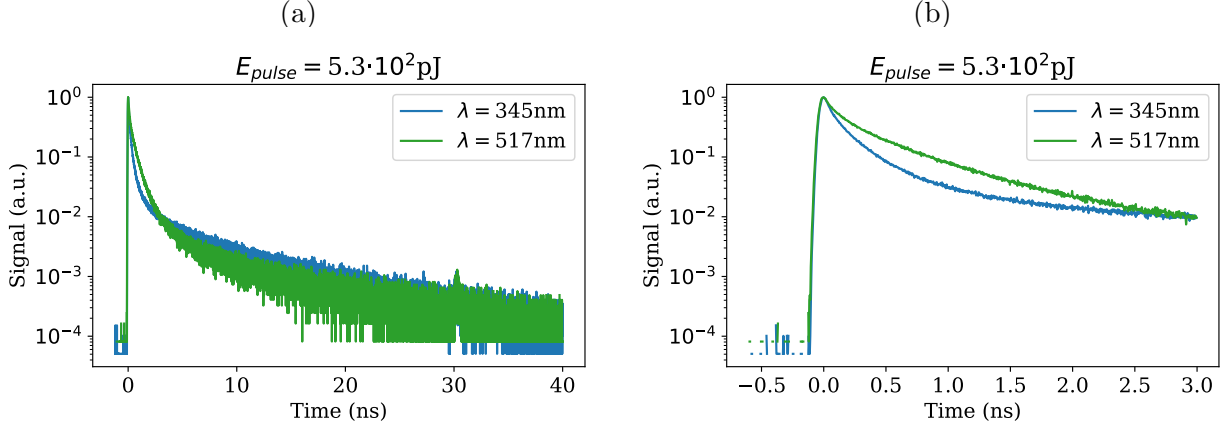

Figure 39: Comparison of GaAs PL decay traces at different excitation wavelengths, but at the same energy per pulse. The peak for the $\lambda = 517$ nm decay trace (green) is much wider than the $\lambda = 345$ nm trace (blue).

5 Conclusion

This research has investigated the carrier dynamics in Cu_2ZnSnS_4 and GaAs. More specifically, we have looked at the fast-electron induced carrier dynamics in these materials. As comparative measurements, we have also studied optically induced carrier dynamics in the same materials. All measurements were based on the luminescence that is produced as the carriers recombine (either cathodoluminescence or photoluminescence).

We have presented a theoretical framework, in which we first calculated carrier generation, both optically and by fast electrons. Secondly, we present a model including the three main types of recombination mechanisms (Shockley-Read-Hall, bimolecular, Auger) and discuss how they relate to the luminescent signal observed in a CL/PL time-resolved measurements. We finally discuss several scenarios from that model, both with analytical and numerical simulations.

We have performed measurements on both GaAs and CZTS with electron and laser excitation. All measurements have been performed in a scanning electron microscope, which can be driven by ultraviolet femtosecond laser pulses to produce bunches of fast electrons. For the PL experiments, we have used femtosecond laser pulses at varying wavelengths to excite our samples.

Both in CL and PL measurements we have done time resolved single photon counting measurements. These measurements were performed as a function of number of electrons per pulse (N_e) and acceleration voltage (U) in the case of CL, or laser pulse energy (E_p) and excitation wavelength (λ) for PL. Additionally, we have measured both CL and PL spectra, using a visible/near-infrared spectrometer.

For the measurements on the CZTS sample, we have used the model presented in the theory section to both qualitatively and quantitatively analyze our data. We have found that, in the regimes of N_e and U that we have measured at, radiative recombination is the dominant recombination channel. This is also the main recombination channel in the case of PL experiments in the regime of E_p and λ that we have measured at. The relevant parameter in this type of recombination is called the bimolecular coefficient (B). We have determined that, in the case of CL experiments on CZTS, the bimolecular coefficient follows a power law as a function of number of electrons per pulse, $B \propto N_e^{-1.1}$. In the case of PL experiments, B is a constant, and we have determined the value to be $B = (4.8 \pm 0.2) \cdot 10^{-10} cm^3 s^{-1}$. This value is on the same order of magnitude as that of the same coefficient for similar materials. To the best of our knowledge, this is the first time that the B coefficient has been determined for CZTS.

Even though the model that we have used for the CZTS is relatively simple, it has allowed us to extract results that make sense in the case of PL. In the case of CL experiments, the interpretation of our results is not as straightforward. It seems as though there are several processes hidden behind the variable B parameter, and this is something that needs additional research.

We have provided a qualitative, and partially quantitative, analysis of the data that we have gathered in our experiments on the GaAs sample. GaAs decay traces can not be reasonably described using our ABC model, but they can, to a reasonable extend, be fitted with

two exponential functions. These are characterized by a short and a long lifetime. In CL experiments on GaAs, both of these lifetimes scale with increasing N_e. We observe a similar trend in PL experiments, but with increasing E_p.

Both the acceleration voltage in CL experiments and the excitation wavelength in PL experiments have a considerable impact on the shapes of GaAs decay traces. The differences between the decay traces from CL and PL experiments for GaAs were also much larger than those for CZTS experiments. We theorize that these differences are mainly caused by a combination of diffusion of carriers and surface recombination. Since the excitation volume is much smaller for CL experiments than it is for PL experiments, diffusion will play a much larger role here. For the same reason, diffusion will play a larger role in the case of smaller acceleration voltages compared to higher voltages in CL experiments. These reasonings are in qualitative agreement with the results from the CL and PL experiments at different voltages and excitation wavelengths. Furthermore, we have reason to believe that a process known as super-diffusion plays a significant role in the experiments on GaAs.

It is remarkable that carrier diffusion and surface recombination play such a significant role in the carrier dynamics in GaAs, while seemingly not playing a significant role in CZTS. We believe that this is due to the fact that our CZTS sample is a polycrystalline material. The grain boundaries might suppress diffusion of carriers, making it easier to model the carrier dynamics using the ABC-model.

Overall, we have studied the main recombination mechanisms in both CZTS and GaAs after excitation by fast electrons and after optical excitations. We have successfully described, both qualitatively and quantitatively, the carrier dynamics in these materials, using the recombination mechanisms that are outlined in the theory section. The results show that while there are some similarities between carrier dynamics in both CL and PL, there are also some differences, linked to the different nature of the excitation. This work provides a a first step into understanding better carrier dynamics after electron excitation, and how it compares to well-known optical excitations.

References

[1] A. Polman, M. Knight, E.C. Garnett, B. Ehrler, W.C. Sinke, "Photovoltaic materials: Present efficiencies and future challenges", *Science, vol. 352* (2016).

[2] C. Persson, "Electronic and optical properties of Cu_2ZnSnS_4 and $Cu_2ZnSnSe_4$", *Journal of applied physics, 107* (2010).

[3] M. I. Hossain, "Prospects of CZTS solar cells from the perspective of properties, fabrication methods and current research challenges", *Chalcogenide Letters, Vol. 9, No. 6* (2012).

[4] L.Q. Phuong, M. Okano, Y. Yamada, A. Nagaoka, K. Yoshino, Y. Kanemitsu, "Photocarrier localization and recombination dynamics in Cu2ZnSnS4 single crystals", *Applied Physics Letters, vol. 103* (2013).

[5] M. Merano, S. Sonderegger, A. Crottini, S. Collin, P. Renucci, E. Pelucchi, A. Malko, M. H. Baier, E. Kapon, B. Deveaud, J.-D. Ganière, "Probing carrier dynamics in nanostructures by picosecond cathodoluminescence", *Nature, vol. 438* (2005).

[6] M.S. Bronsgeest, "Physics of Schottky electron sources", PhD dissertation, Technical University Delft (2009).

[7] S. Meuret, M. Solà Garcia, T. Coenen, E. Kieft, H. Zeijlemaker, M. Lätzel, S. Christiansen, S.Y. Woo, Y.H. Ra, A. Polman, "Complementary cathodoluminescence lifetime imaging configurations in a scanning electron microscope", *Ultramicroscopy 197 pp. 28-38* (2019).

[8] C. Kittel, "Introduction to solid state physics, 8th edition", *Wiley, ISBN 0-471-41526-X* (2005).

[9] D.J. Griffiths, "Introduciton to electrodynamics 4th edition", *Cambridge University Press. ISBN 9781108420419* (2013).

[10] E. D. Palik, "Handbook of Optical Constants of Solids", *Academic Press* (1998).

[11] D. E. Aspnes, S. M. Kelso, R. A. Logan, R. Bhat, "Optical properties of $Al_xGa_{1x}As$", *Journal of Applied Physics vol. 60, $754-767$* (1986).

[12] N. Bakr, Z. Khodair, H. Mahdi, "Influence of Thiourea Concentration on Some Physical Properties of Chemically Sprayed Cu2ZnSnS4 Thin Films" *International Journal of Materials Science and Applications vol. 5 261-270* (2016).

[13] H. Raether, "Excitation of Plasmons and Interband Transitions by Electrons", *Springer: Tracts in modern physics, 88* (1980).

[14] R.F. Egerton, "Electron energy-loss spectroscopy in the TEM", *Reports on Progress in Physics, 72* (2009).

[15] R.F. Egerton, M. Malac, "EELS in the TEM", *Journal of electron spectroscopy and related phenomina,* **143**(2005).

[16] C.A. Klein, "Radiation ionization energies in semiconductors: speculations about the role of plasmons", *Journal of the physical society of Japan, vol.* **21***, suppl.* (1966).

[17] H. Demers, N. Poirer-Demers, A.R. Couture, D. Joly, M. Guilmain, N. de Jonge, D. Drouin, "Three-dimentional electron microscopy simulation with the CASINO Monte Carlo software", *Scanning, vol.* **33** (2011).

[18] M.L. Brongersma, N.J. Halas, P. Nordlander, "Plasmon-induced hot carrier science and technology", *Nature Nanotechnology,* **10** (2015).

[19] A. rothwarf, "Plasmon theory of electron-hole pair production: efficiency of cathode ray phosphors", *Journal of applied physics,* **44** (1973).

[20] B. Rethfeld, "Unified model for the free-electron avalanche in laser-irradiated dielectrics", *Physical review letters, vol.* **92***, nr.* **18** (2004).

[21] S.M. Sze, "Physics of semiconductor devices, 2nd edition", *Wiley, ISBN:9780471143239* (1981).

[22] M. De Laurentis, A. Irace, "Optical measurement techniques of recombination lifetime based on the free carrier absorption effect", *Journal of solid state physics, 291469* (2014).

[23] I. Pelant, J Valenta, "Luminescence Spectroscopy of Semiconductors", *Luminescence Spectroscopy of Semiconductors, pp. 1-560* (2012).

[24] U. Strauss, W.W. Rühle, K. Köhler, "Auger recombination in intrinsic GaAs", *Applied Physics Letters* **62** *(1)* (1993).

[25] M.w. Gerber, "Recombination mechanisms in gallium arsenide", *PhD Thesis, McMaster University* (2016).

[26] H. Schlangenotto, H. Maeder, W. Gerlach, "Temperature dependence of the racombination coefficient in silicon", *Physica Status Solidi (a), vol.* **21** (1974).

[27] A. David, N.G. Young, C. Lund, M.D. Craven, "Review - the physics of recombinations in III-nitride emitters", *ECS Journal of Solid State Science and Technology,* **9** (2020).

[28] W. Liu, R. Butté, A. Dussaigne, N. Grandjean, B. Deveaud, G. Jacopin, "Carrier-density-dependent recombination dynamics of exitons and electron-hole plasma in m-plane InGaN/GaN quantum wells", *Physical Review B, vol.* **94** (2016).

[29] A. David, M.J. Grundmann, "Droop in InGaN light-emitting diodes: A differential carrier lifetime analysis", *Applied Physics Letters, vol.* **96** (2010).

[30] B.A. Ruzicka, L.K. Werake, H. Samasessekou, H. Zhao, "Ambipolar diffusion of photoexcited carriers in bulk GaAs", *Applied Physics Letters vol.* **97** (2010).

[31] D.D. Nolte, "Surface recombination, free-carrier saturation and dangling bonds in InP and GaAs", *Solid-State Electronics, vol. 33 nr. 2* (1990).

[32] A.B. Sproul, "Dimensionless solution of the equation describing the effect of surface recombination on carrier decay in semiconductors", *Journal of Applied Physics, vol. 76, n. 5* (1994).

[33] T. Coenen, "Angle resolved cathodoluminescence nanoscopy", PhD dissertation, University of Amsterdam (2014).

[34] D. Yang, O.F. Mohammed, A.H. Zewail, "Scanning ultrafast electron microscopy", *Proceedings of the National Academy of Sciences, 107 (34) 14993-14998* (2010).

[35] A. Feist, N. Bach, N. Rubiano da Silva, T. Danz, M. Möller, K.E. Priebe, T. Domröse, J.G. Gatzmann, S. Rost, J. Schauss, S. Strauch, R. Bormann, M. Sivis, S. Schäfer, C. Ropers, "Ultrafast transmission electron microscopy using a laser-driven field emitter: Femtosecond resolution with a high coherence electron beam", *Ultramicroscopy 176 pp. 63-73* (2017).

[36] M. Wahl, "Time-Correlated Single Photon Counting", *Technical note PicoQuant* (2014).

[37] P. van Capel, E. Langereis, W. Westerveld, "Data-acquisitie en Toegepaste analyse", (2013).

[38] R.K. Ahrenkiel, B.M. Keyes, D.J. Dunlavy, "Intensity dependent minority carrier lifetime in III-V semiconductors due to saturation of recombination centers", *Journal of Applied Physics, vol. 70* (1991).

[39] C. R. Haughn, K. J. Schmieder, J. M. O. Zide, A. Barnett, C. Ebert, R. Opila, M. F. Doty, "Quantification of trap state densities in GaAs heterostructures grown at varying rates using intensity-dependent time resolved photoluminescence", *Applied Physics Letters, vol. 102* (2013).

[40] E. Najafi, V. Ivanov, A. Zewail, M. Bernardi, "Super-diffusion of excited carriers in semiconductors", *Nature Communications, 15177* (2017).

[41] K. Chen, W. Wang, J. Chen, J. Wen, T. Lai, "A transmission-grating-modulated pump-probe absorption spectroscopy and demonstration of diffusion dynamics of photoexcited carriers in bulk intrinsic GaAs film", *Optics Express, 3580* (2012).

[42] D. Steiauf, E. Kioupakis, C.G. Van de Walle, "Auger Recombination in GaAs from First Principles", *ACS Photonics 1, 643 - 646* (2014).

A   Appendix: Harmonic generator

An important part of our experimental setup is the harmonic generator (HG). The setup of the HG is schematically shown in figure 40.
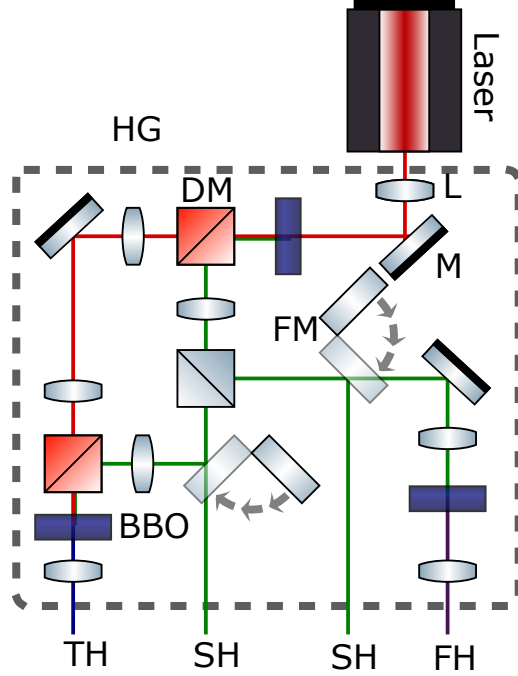

Figure 40: The harmonic generator is shown schematically within the dashed gray lines. In the top right, the fundamental beam (red) enters the HG. At the bottom, the SH (green), TH (blue) and FH (violet) beams leave the HG.

We use an Yb-doped fiber femtosecond laser (Clark MXR) that generates Gaussian pulses at a wavelength of 1034 nm (fundamental, red in figure 40) with a pulse duration of 250 fs. Pulses produced by the laser are first partially frequency doubled by a beta barium borate (BBO) crystal (blue rectangle in figure 40). This results in the generation of a laser beam at 517 nm (second harmonic, SH, green in figure 40). Part of the fundamental beam is not converted due to the limited efficiency of the BBO crystal. A dichroic mirror (DM) splits these two beams by reflecting the SH and letting the fundamental pass through. The SH pulses pass through a half-wave plate (not shown) and a polarizing beam splitter (PBS). With this configuration the SH beam is split into two separate beams, each directed towards a different path. The power ratio of these two beams is modulated using the aforementioned half-wave plate. In the first path, the beam is either guided directly out of the HG using a flip mirror (FM), or towards another BBO crystal (X3). At this crystal, the SH beam is combined with the left-over fundamental beam to create a beam at a wavelength of 345 nm (third harmonic, TH, blue in figure 40), which is lead directly out of the HG. The other SH beam can be guided towards yet another BBO crystal. This crystal doubles the frequency of the SH beam to generate a beam at a wavelength of 258 nm (fourth harmonic, FH, violet in figure 40). The FH beam is directly guided out of the HG. If the flip mirror before this BBO crystal is engaged, the SH pulses are lead out of the HG.

B   Appendix: CZTS B coefficient map

If we want to know the value of the B parameter for CZTS, it is important to check whether this value is dependent on the excitation location. In order to determine if this is the case, we have measured 64 CL decay traces covering an area of 10 μm by 10 μm. We used an acceleration voltage of 30 kV, an integration time of 60 s and the number of electrons per pulse was approximately 90 (although this value changed somewhat throughout the experiment). Located in the upper right corner of this area was a dust particle. We expect the value of B not to change on the CZTS sample, but to be either different or non-determinable on the dust particle. Figure 41 shows the fitted value of $B\Delta n_0$ as a function of position along with the error.
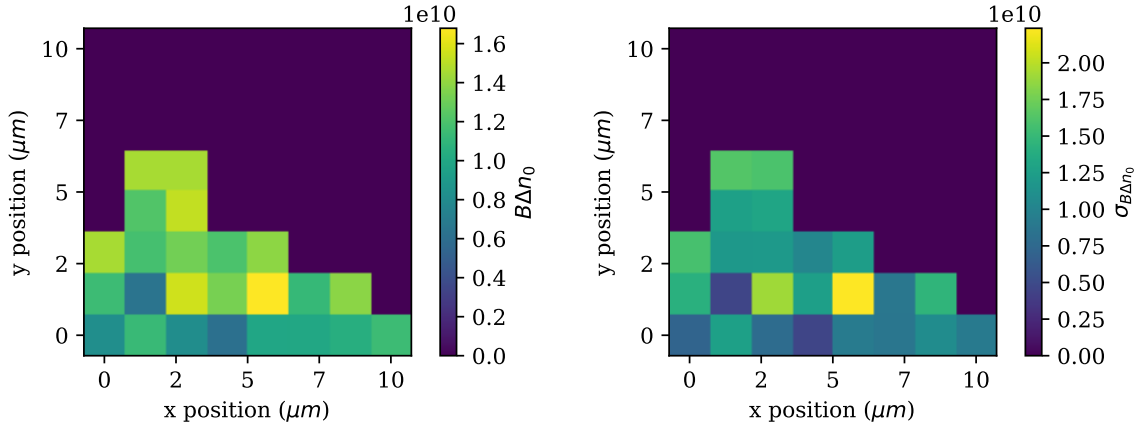

Figure 41: Left: map of the ideal fit value of $B\Delta n_0$ of CZTS with a dust particle. Right: the error in the fit parameter.

It seems as though the value of $B\Delta n_0$ does not significantly change. The signal to noise ratio is however very low for these traces, resulting in very large errors. For this reason, we can not definitively conclude that B is not a function of the location on the sample, even though it seems that it it does not depend on the location.